Investigation of resonant effects in core-shell metasurface geometries and design concept of a metasurface for harmonic generation

Master's Degree Project

Performed at Synchrotron Radiation Research Division and Atomic Physics Division

Department of Physics, Lund University

Samuele Marzanati

Supervisor: Matias Kagias

Co-Supervisor: Cord Arnold

Popular Science Abstract

Controlling and generating light has always been a goal of humanity, long before anyone understood what light actually was. But it is only "recently", during the last few centuries, that we "shed some light" on the origins of colors, rainbows, the blue sky, and how mirrors and lenses can reflect and bend the light. For over 200 years, researchers have been studying the interaction between light and materials, culminating in the recent developments of metasurfaces.

Metasurfaces are new type of very thin artificially designed materials whose surfaces are composed of tiny structures arranged in a regular array, and that are capable of achieving optical properties that are beyond those seen in materials found in nature. This patterned surface can be seen as a mosaic, in which the structures, called meta-atoms, are the individual ceramic pieces. In a mosaic, the complex arrangement of the pieces is indistinguishable, but when viewed from a distance the composition reveals a coherent and beautiful image. Metasurfaces work in a similar way, even if not visible to the naked eye, the tiny meta-atoms on the surface are what enable researchers to manipulate light with unprecedented control in such a thin device.

In metasurfaces however, the design of the meta-atoms is crucial to achieve the correct functionality, and to strongly interact with the light that is visible to the human eye, their dimensions had to be shrunk down to a size hundreds of times smaller than the width of a human hair. At these scales, each meta-atom can interact with light in a precise and controlled way, but collective resonant effects where the light interact with the whole patterned surface are also possible. By carefully designing the geometry and the materials in use, researchers were able to create devices that focus light without curved lenses, encode images and generate additional light colors from a laser beam emitting light at only one color.

Many different shapes and geometries have been investigated, but this project will focus on one design opportunity that has not been explored yet. Instead of building the meta-atoms from a single material, the meta-atoms studied in this thesis are formed by a core cylindrical pillar of one material wrapped by a shell of another, forming what is called a core-shell geometry. The goal is to investigate how this structure affects the way the metasurface interact with light and this thesis will show how combining two dielectric materials can offer a new degree of freedom for tuning the optical response. In addition, a second goal is to create a metasurface design that by exploiting the resonances, it would be capable of generating light at a higher energy than the incoming laser beam, in a process called harmonic generation.

To achieve these goals, computers helped in simulating the behaviour of the studied metasurfaces without the need to create and test each design. Two designs were then chosen to be fabricated using modern nanotechnology tools and their response, obtained by illuminating them with light, was measured and compared against the simulations.

Abstract

Metasurfaces are two-dimensional arrays of sub-wavelength structures often arranged in a periodic lattice. During recent years, metasurfaces have emerged as one of the most promising platforms to shape electromagnetic waves using compact devices, exhibiting extraordinary control over the light amplitude, polarization and phase. Starting with metallic materials, metasurface research has shifted toward dielectric-based devices to achieve low losses and enable control of light in the visible spectrum, with new functionalities emerging from complex resonant effects within the scatterers. Resonant metasurfaces provide a new platform to engineer the electromagnetic response, and the ease of fabrication allowed researchers to explore a variety of new designs over the years for many different applications, including harmonic generation. While some materials of choice have been identified for specific applications and spectral ranges, new approaches based on hybrid material compositions have been lacking and could offer new degrees of freedom for tuning the resonances without modifying the scatterers geometry. This thesis investigates the resonant response of all-dielectric metasurfaces composed of meta-atoms with a core-shell structure, in which a cylindrical pillar of one material is coated by a shell of a second material. The scattering and resonant response of single meta-atoms and metasurfaces having a core-shell geometry are studied using finite element simulations, investigating how the shell thickness, pillar diameter, height and periodicity affect the resonant behaviour of the devices. Two metasurfaces are fabricated using electron beam lithography and atomic layer deposition and are optically characterized using a white light source. In parallel, a metasurface concept optimised for third hamornic generation is designed to be placed inside a multicell pass to increase the efficiency of the nonlinear process.

Acknowledgements

I would like to thank my supervisor Matias and co-supervisor Cord for their help and guidance. Over the past year I got to learn a lot of new concepts and methods and their support and availability made this project an enriching experience.

I also want to thank the PhD students and postdocs in the group, Jeevan, Gustavo, Christopher and Zesen for their immense help both in the cleanroom and with the simulations. I felt very lucky to work alongside you and learn from you. I also want to thank Chen for his great help in building and calibrating the interferometer.

I want to thank my family, who made this experience possible and who have always supported me and believed in me, this achievement is yours too. I want to thank Alice for her love and for being my greatest motivation, even when things were hard, I am grateful to have had you by my side, I love you. Thank you to Johannes and Hilya for being the best friends I could have hoped to find in Lund, I was very lucky to meet you and share this experience with you. Thank you to Lixuan for the laughs, the talks, the parties and the dinners together, it was wonderful to share these two years with someone who has the same interests and passions. Thank you to Sara, Yuhao, Dorota and everyone else in my programme, it was a lot of fun taking classes, struggling and celebrating together. Last but not least, I want to thank everyone at the Greenhouse for making this last year incredibly fun, I only wish I had met you sooner. And thank you to all the people I met here in Lund and to all the teachers who taught me so much over these two years. Thank you all.

Contents

1 Introduction **1**
1.1 Objective . . . 4
1.2 Thesis Outline . . . 5

2 Theory **6**
2.1 Resonant Metasurfaces . . . 6
2.2 Mie Resonances . . . 9
2.2.1 Lattice Resonances . . . 12
2.3 Nonlinear Optics . . . 13
2.3.1 Second and Third Harmonic Generation . . . 13
2.3.2 White Light Generation . . . 14

3 Methods **16**
3.1 Simulations . . . 16
3.1.1 Finite Element Method (FEM) and the Weak Formulation . . . 16
3.1.2 Simulations Workflow . . . 18
3.1.3 Simulation of the meta-atoms scattering response . . . 20
3.1.4 Simulation of the metasurfaces resonant response . . . 21
3.2 Fabrication . . . 22
3.3 White Light Spectroscopy . . . 26

4 Results and Discussion **27**
4.1 All-dielectric Resonant Metasurfaces . . . 28
4.1.1 Meta-atoms Scattering . . . 28
4.1.2 Geometrical Parameters Study . . . 32
4.2 Metasurfaces for Nonlinear Optics . . . 39
4.2.1 TiO_2 Resonant Metasurface . . . 39
4.2.2 HfO_2 Resonant Metasurface . . . 41
4.3 Fabrication . . . 45
4.4 Optical Characterization . . . 47

5 Conclusions and Outlook **51**

References **53**

1 Introduction

Metamaterials are a class of materials designed to achieve new and unique functionalities that are not normally found in nature. In fact, the prefix *meta* comes from the Greek word for "beyond" to signify the peculiar properties of these artificial materials, which extend beyond what is possible for conventional materials.

Even though the term *metamaterial* was first introduced in 1999 by Rodger M. Walser in a DARPA Workshop, examples of similar unconventional materials can be found in nature, like the interference effects caused by the structured protein patterns that constitute the wings of some species of butterfly, as well as in ancient human artefacts like the Lycurgus cup (Fig. 1), where dichroism is induced by the distribution of gold and silver nanoparticles inside the glass.

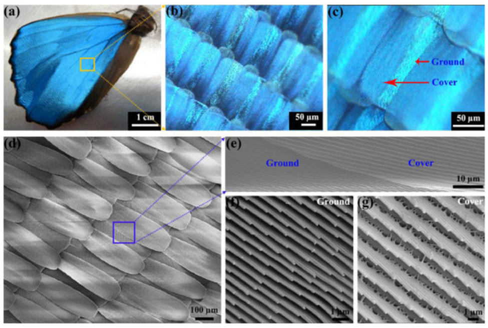

(a)

(b)

Figure 1: Two metamaterial examples. (a) The interaction between light and the periodic protein nanostructures in butterfly wings produces vibrant colours. This phenomenon, known as structural coloration, arises from light interference rather than pigments [1].(b) The Lycurgus cup is made of a type of dichroic glass which turns green when seen from reflected light to ruby red when backlit. The dichroism is caused by gold and silver nanoparticles in the glass that scatter light differently depending on the illumination[2].

The structure of a metamaterial is composed by three-dimensional subwavelength building blocks, often referred to as *meta-atoms*, that can be tuned and designed to achieve new fascinating optical properties. One of the most prominent and impactful examples is the possibility to design materials with negative refractive indexes, a concept firstly described mathematically by Veselago[3] in 1968, and successively demonstrated by Shelby[4] et al. in 2001 using metallic structures. Metamaterials gained significant momentum in the early 2000s, with a focus on materials with near-zero refractive index and tunable effective permittivity and permeability. At that time, the research efforts were pushed by the theoretical prospect of using metamaterials to achieve electromagnetic cloaking, however the lack of broadband capabilities has so far precluded any practical implementation of this technology.

While the initial enthusiasm for metamaterials declined after the first decade of the 21st century, their 2D counterpart, referred as *metasurfaces*, started to gain traction. Metasurfaces consist of 2D arrays of meta-atoms usually placed on a thin substrate. Their planar nature greatly simplifies the fabrication process, their scalability toward lower working wavelengths and the integration with compact optical systems. Moreover, metasurfaces have lower losses compared to metamaterials due to their inherent thin structure[5]. The precursors of this technology can be dated back to the 1990s, when arrays of resonant metallic microstrips were introduced in reflectarrays and transmitarrays to shape the phase profile of wavefronts in the microwave spectrum.[6] Nonetheless, early metasurfaces operated in the mid infrared and relied on metallic meta-atoms and plasmonic resonances, achieving prominent landmarks like the demonstration of anomalous refraction, beam steering, flat lensing, perfect absorbance and holography [7, 8, 9].

However, extending this framework to near-infrared and visible wavelengths required reducing the meta-atom dimensions to the nanoscale in order to remain in the subwavelength regime, and the field's rapid expansion since then has been closely linked to the advances in nanofabrication technology and its wider accessibility.

In the last decade, the research has shifted from metallic metasurfaces to dielectric ones. This change has been motivated by the numerous advantages that dielectric metasurfaces have compared to their metallic counterparts, comprising superior efficiency, lower losses, larger meta-atoms dimensions and multipole resonances in single meta-atoms capabilities[5, 10]. Instead of plasmonic resonances, which are governed by the collective oscillations of electrons, dielectric metasurfaces exploit Mie resonances, a scattering phenomenon first demonstrated by the homonymous scientist in 1908[11] in which the incident electromagnetic field drives displacement currents inside the dielectric particles, exciting spectrally distinct electric and magnetic multipolar modes whose interference determines the properties of the scattered light.

Over the years, dielectric metasurfaces have become the preferred platform in the field for applications in the visible and infrared spectral range, with uses in imaging[12], holography[13], nonlinear optics [14], ultrafast optics[15] and integrated photonics[16]. A number of dielectric materials and designs have been tested, with high-index meta-atoms attracting particular interest for applications across the ultraviolet to the infrared spectral range. In particular, Si-based metasurfaces have been extensively used in the near-infrared due to the low extinction and high efficiency of silicon in this region, while TiO_2-based metasurfaces have become the best candidate for research in the visible range due to the high refractive index and low exctinction coefficient of the material[17].

One of the most promising applications for metasurfaces is flat optics. Enabled by the tunable phase delay imparted by each meta-atoms, the metasurface can precisely shape the wavefront locally over its flat surface, efficiently focusing the light without the need for curved lenses or mirrors. Designing the meta-atoms to achieve full-phase coverage is essential to prevent wavefront aberrations, and while some examples of 2π-phase coverage and polarization control were achieved by carefully choosing the correct refractive index and height of the meta-atoms, with the phase delay governed by the accumulated optical path length through the structure[18, 12], new functionalities can arise from exploiting the abrupt phase change that happens when the incoming radiation interacts with the resonant modes of the meta-atoms. For example, a 2π phase change within a narrow bandwidth is achievable when both the electric and magnetic dipoles are excited in the structure, causing a π phase shift for each resonance.

Furthermore, by tuning the geometry of the resonant meta-atoms, one could realize a so called Huygens' metasurface, in which the interference between the two dipoles is destructive in the backscattered direction and constructivein the forward direction respectively. An all-dielectric metasurface of this kind for the NIR frequencies was demonstrated in 2015 for the first time by Decker et al.[19], where silicon nano-disks with overlapping resonances achieved a 55% transmission efficiency at around 1250 nm.

As in the previous example, resonant metasurfaces can display many exotic resonant phenomena when different modes get excited and interfere, and have become one of the preferable platform in the nanophotonics field, with new applications and behaviours not achievable by conventional optics. Dielectric resonant metasurfaces can be fabricated to observe quasi Bound States in the Continuum (qBIC), Fano resonances, anapole resonances and lattice resonances, and due to the use of dielectric materials, researchers have been exploring new geometries and designs that had been precluded by the intrinsic losses in metallic metasurfaces.[10].

In recent years, resonant metasurfaces have been explored as a platform to observe and drive nonlinear optical effects in thin layers of material. In fact, the high field enhancements induced by the Mie-type resonances and their interference can be exploited to boost nonlinear interactions inside the dielectric material at achievable light intensities. Moreover, low losses and high damage thresholds, dielectric resonant metasurfaces have additional advantages for harmonic generation, even compared to bulk materials[20]. The most important property of using dielectric metasurfaces for nonlinear effects is that their thin dimensions allow for relaxed phase-matching conditions. For example, the coherence length of GaN, one of the materials used for second harmonic generation (SHG), is in the range of 1-10 μm [21], which is compatible with most meta-atom's dimensions in the literature. The reduced thicknesses of the metasurfaces decrease the nonlinear efficiency, but the field enhancement caused by the resonances can partially compensate for this loss.

SHG is a nonlinear effect governed by the $\chi^{(2)}$ susceptibilty tensor, which vanishes in materials having centrosymmetric structures due to the electric field and polarization opposite parities. For this reason, only non-centrosymmetric crystals, where this material symmetry is broken, can have $\chi^{(2)} \neq 0$. Many different non-centrosymmetric crystals have been explored for fabricating metasurfaces to work in the nonlinear regime, including SiC, ZnO, GaN, LiNbO3, with high emphasis on $III - V$ semiconductors such as GaAs and AlGaAs due to their high second-order nonlinear coefficient, which could increase the SHG efficiency by 10^4 compared to an unstructured material film [22].

For third harmonic generation (THG) instead, the missing non-centrosymmetric requirement enables a wide choice of possible materials, but the wide availabilty of nano-processing technologies and techniques for Si and its high third-order nonlinear susceptibility $\chi^{(3)}$ has made silicon the material of choice for THG metasurfaces research. BICs and Fano resonances can be exploited to achieve high field enhancements and Q-factors, with the choice of material and geometrical parameters dictating the resonance spectral locations.

The main downside of nonlinear metasurfaces is that by exploiting such narrow resonances, their broadband capabilities are inherently limited, and high field enhancement is generally achieved by exploiting non-locality, making the resonances dependent on more parameters such as the light polarization and its angle of incidence. Recent advances have begun to address these trade-offs through both material and geometric strategies. Incorporating monolayer materials such as WSe_2 on top of the metasurface has proven effective in boosting SHG while also exploiting the angular dependence of BICs[23], whereas carefully engineered geometries can favor local resonances whose response remains largely insensitive to polarization and angle of incidence[14].

All-dielectric resonant metasurfaces have been established as a flexible and promising framework to control multiple properties of light as shown in the examples above. Due to their inherent functionality, resonant metasurfaces are generally designed to work with a narrower bandwidth compared to their non-resonant equivalents, even if some more complex designs can relax this constraint[24]. Furthermore, reducing meta-atom dimensions to the quantum scale may unlock new resonant phenomena and electromagnetic wave control[25].

Nonetheless, new approaches to control and study the resonant response of metasurfaces by implementing more than one dielectric material in the meta-atom structure have been lacking. Enabled by modern fabrication techniques, the creation of hybrid dielectric meta-atoms could pave a new way to tune the resonances and increase the confinement of the electromagnetic fields inside the meta-atoms. Borrowing an established definition from the nanoparticle research, such structures can be realized, as illustrated in Fig. 2, in a *core-shell* geometry, where a dielectric pillar of one material is coated by a shell made of a second dielectric, offering a new degree of freedom in metasurface design to tune the resonant modes without affecting the geometry or the periodicity.

In addition, given the advantages that metasurfaces have over bulk material in harmonic generation, new designs and platforms are needed to expand the research on increasing the nonlinear efficiencies obtained through the use of metasurfaces as the interaction medium. For example, recent advances have shown that the integration of metasurfaces with a multipass cell can enhance the nonlinear response by an order of magnitude[26].

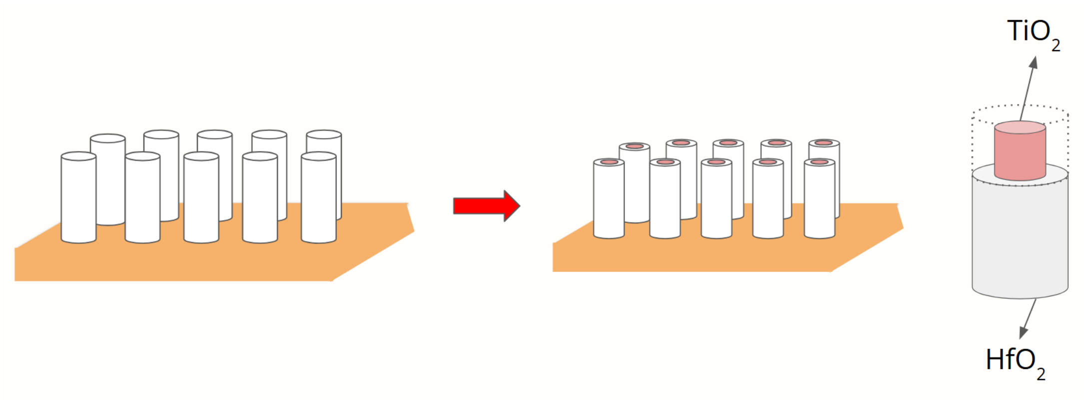

Figure 2: Illustration of example core-shell metasurface composed of meta-atom pillars having a TiO_2 core and an HfO_2 shell.

1.1 Objective

This thesis pursues two main goals. The first goal is to investigate and study the resonant response of dielectric metasurfaces, comparing single-material and core-shell meta-atom designs to understand how the introduction of the core-shell structure affects the resonant behaviour of the devices. The second goal of this thesis is to design a dielectric resonant metasurface optimised for third harmonic generation and intended to be integrated within a multi-pass cell configuration to increase the THG efficiency.

1.2 Thesis Outline

First, Chapter 2 will introduce the theory underlying this thesis, including a general classification for metasurfaces, a brief introduction of Mie theory and the resonant modes supported by dielectric meta-atoms, including how these can interfere with each other to produce new fascinating resonant features. This chapter will conclude with an overview of the nonlinear optical effects pertinent to the thesis. Afterwards, Chapter 3 will describe the numerical, fabrication and optical characterisation methods employed throughout the thesis, including the electromagnetic simulation framework used to model the meta-atom and metasurface response, the fabrication processes involved to realise the metasurfaces and a description of how the spectroscopy setup was implemented in order to characterize the resonant response of the fabricated metasurfaces. Finally, Chapter 4 will present the simulation results for both single-material and core-shell meta-atom and different metasurface designs, with emphasis on how the core-shell geometry affects the resonant behaviour, together with the design and simulation process that was done to create a metasurface concept intended for third harmonic generation inside a multi-pass cell. This final chapter also includes the fabrication outcomes of the two metasurfaces realized at Lund NanoLab, as well as the results from their optical characterization, performed at the Atomic Physics Division, and achieved by using a white light spectroscopy setup.

2 Theory

In this chapter, the theoretical background relevant to this thesis is introduced. Starting from a general classification of metasurfaces, the discussion will then cover how the geometry and the choice of material can generate to resonant effects in all-dielectric metasurfaces and how the interference between those resonances can give rise to interesting optical phenomena. The last part will focus on nonlinear optics, including second and third harmonic generation and white light generation.

2.1 Resonant Metasurfaces

The term *metasurface* has been applied to a variety of devices with many different applications, and it is possible to find examples of this technology in the literature that don't necessarily fit the definition that has been given in this thesis for what a metasurface is. Nevertheless, to better understand the scope of this thesis, a classification for metasurfaces readapted from [27, 28] will be introduced here.

Depending on the operational wavelength λ and the periodicity Λ of the meta-atoms, one can distinguish three main regions in which any metasurface could be placed, depending on the parameter Λ/λ. This first classification based on the geometrical parameters is depicted in Fig. 3.

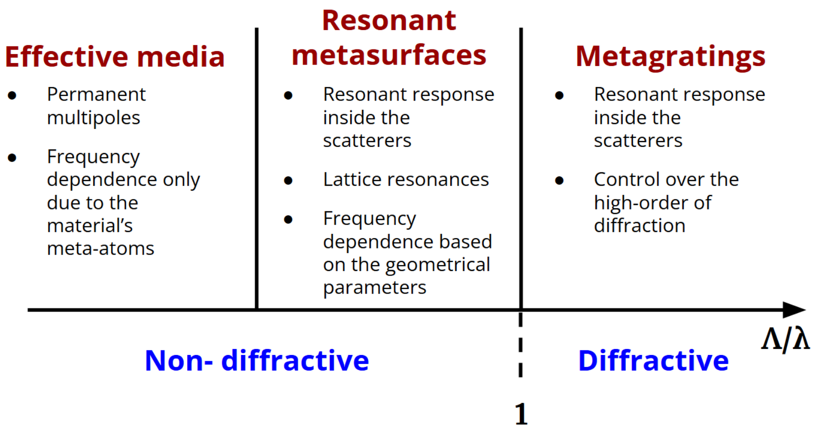

Figure 3: Metasurfaces classification based on geometrical parameters.

- **Region 1 - Effective Media:** In this region, the operational wavelength is much larger than the separation between the meta-atoms and the meta-atoms themselves. The scatterers could be seen like atoms or molecules in a generic material, inducing permanent dipole moments that could be designed to create an artificial composite material. The metasurfaces in this region can be approximated as effective media with homogeneous material properties obtained from quasi-static solutions applied to the periodic structure. Many different types of formulas can be found in the literature to model the effective material parameters of this kind of metasurfaces[29, 30], but all of them share the use of approximations valid when $\lambda >> \Lambda$.

- **Region 2 - Resonant Metasurfaces:** Here, the meta-atom dimensions become comparable to the operational wavelength, and the structure is designed to support and excite specific multipolar resonances. In this region $\lambda > \Lambda$, and it is where the literature most commonly refers to devices by using the term *metasurfaces*. For these materials, the permittivity and the permeability can be considered as effective properties and wavelength dependent due to the resonant response of the scatterers. Additionally, the collective response of the resonators periodically arranged on the surface can give rise to further resonant phenomena, known as *lattice resonances*.

- **Region 3 - Metagratings:** The devices in this region act as gratings, but with additional properties that arise from the resonant response induced by the geometry of the scatterers. In this regime, the meta-atoms are larger than the operational wavelength and $\Lambda \approx \lambda$ or higher. The purpose of these devices is to control the higher diffraction orders. Many different concepts have been realized, achieving high efficiency beam steering at large angles and anomalous reflection[31].

The metasurfaces studied in this thesis will be mainly designed to be in the second region, where the spacing between meta-atoms, together with their geometry, governs the resonant response. Choosing the correct geometry though, is not the only critical parameter to tune the resonant response, the fundamental electromagnetic properties of the metasurfaces are decided by the building material. In fact, metallic-based metasurfaces possess intrinsic thermal loss, which can limit their performance and flexibility.

On the other hand, dielectric metasurfaces have been able to replicate many of the operations achievable by their metallic counterpart, but with lower losses. All-dielectric metasurfaces can simultaneously excite different electric and magnetic multipoles within a single meta-atom, a feature that is difficult to replicate in metallic structures and only achievable with low efficiencies[32].

Two other main groups of metasurfaces can be distinguished based on the scattering response of the meta-atoms: *non-local* and *local*. If the scattering at any surface location is independent of the fields or resonator response located at a different position, the metasurfaces can be defined as local. The meta-atom response can be approximately considered fixed for a given incoming field, even when the surrounding field or scatterers have changed. The narrow locality of the response in the real space leads to a broad response in the reciprocal space, for this reason the so called *local metasurfaces* have a broader bandwidth and the response can be considered approximately independent from parameters such as the light's angle of incidence[14].

On the other hand, in a *non-local metasurface* the scattering response of a meta-atom depends on the fields and the meta-atoms close by, and due to this scattering extended reach in real space, the response in the reciprocal space is narrow, giving rise to sharp resonances with high Q-factors and high dependence on the light angle of incidence. It should be noted that the boundary between these two categories is not strict: local metasurfaces represent simply a limiting approximation of the more general non-local description, and all metasurfaces exist along a continuum of nonlocality, where the local extreme would be represented by a metasurface that acts like an effective medium, while the non-local extreme can be represented by a low contrast grating, i.e. a grating with shallow corrugations and small refractive index contrast with its surroundings.

In general, non-locality is associated with high Q-factors due to the narrow bandwidth of the resonances, while local metasurfaces have a more broadband response. It is then possible to use the degree of non-locality as an additional parameter for classifying resonant metasurfaces and metagratings. A conceptual map that includes geometrical parameters classification and non-locality can be reconstructed as in Fig. 4.

It is important to note that this classification is used in this thesis to better visualise the results, the designs and the scope of the thesis, but as of today, the term metasurface is used in a broad spectrum of devices, and it is possible to find in the literature classifications that diverge significantly from the one shown in Fig. 4 [28].

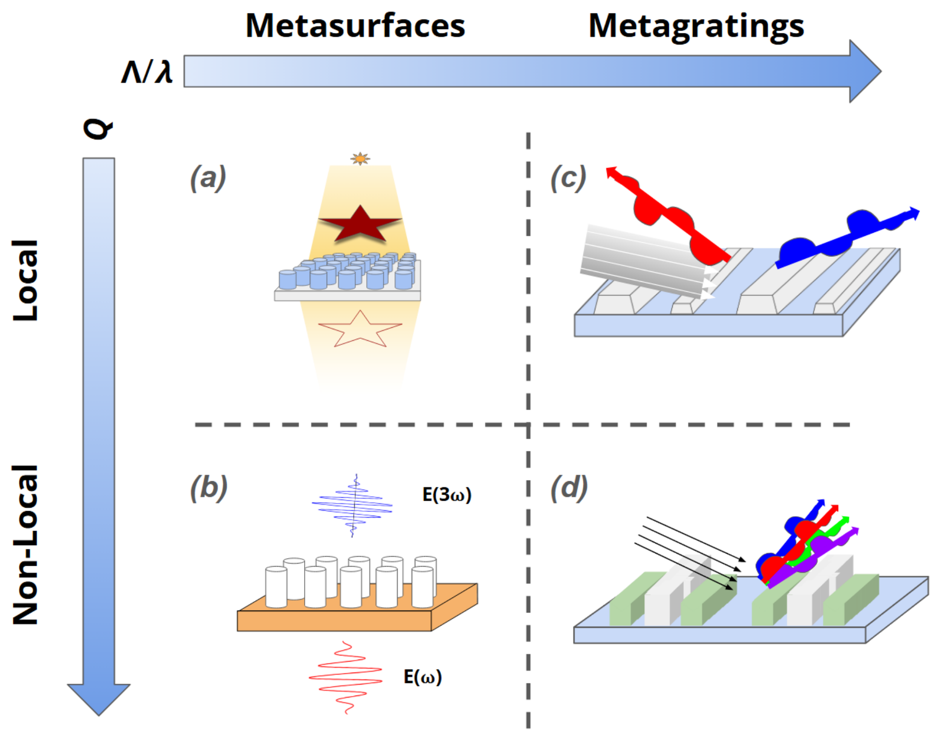

Figure 4: Metasurface and metagratings classification based on Q factor and ratio between the periodicity of the lattice Λ and the operating wavelength λ. Non-local metasurfaces are associated with high Q-factors, while $\Lambda \approx \lambda$ indicates the separation between metasurfaces and metagratings. (a) Metasurfaces with a low Q-factor can be used for image differentiation[33]. (b) Metasurfaces with high Q-factors can enhance the efficiency of third-harmonic generation due to their strong field enhancement within the structure[20]. (c) Metagratings can support anomalous reflection, in which light is reflected at non-specular angles, violating Snell's law[34]. (d) Metagratings with broken-symmetry structures can exhibit high Q-factors that enable control over the efficiency of higher diffraction orders[35].

2.2 Mie Resonances

The meta-atoms that compose an all-dielectric metasurface need to be carefully arranged and designed to achieve the desired electromagnetic control over the incoming light. The scattering response is governed by Mie-type resonances that can be excited depending on the geometrical parameters and choice of materials.

For a resonant metasurface, the meta-atoms' dimensions need to be comparable to the operational wavelength and using high refractive index material for the fabrication is the preferred choice due to the better confinement and coupling with the incoming electromagnetic field.
In fact, following Mie theory for scattering, the first resonance to appear in a dielectric sphere is the magnetic dipole, which can be excited when

$$D \approx \frac{\lambda_0}{n} \tag{1}$$

where D is the diameter of the sphere, λ_0 is the operational wavelength in vacuum and n is the refractive index of the sphere[36]. This law holds approximately regardless of the meta-atom geometry, and it sets a lower limit on the scatterer size when designing a resonant metasurface, making high refractive index materials particularly desirable, as they allow resonances to be excited within more compact structures.

In his paper, Gustav Mie found the solution for the scattering of a plane wave of any wavelength by a sphere of any size[11]. He found that the total scattering cross-section of the particle was in the form of an infinite series that can be expressed as[37]:

$$\sigma_M = \frac{2\pi}{k^2} \sum_{n=1}^{\infty} (2n+1)(|a_n|^2 + |b_n|^2) \tag{2}$$

where $k = 2\pi n/\lambda_0$, and the coefficients a_n and b_n are expressed in terms of spherical Hankel and Bessel functions of the first kind, and respectively represent the contribution from the magnetic and electric multipoles[36]. Even if Mie scattering gives an exact solution only for spherical particles, the term has been used in the field of nanophotonics to indicate the scattering mechanism and the resonances that only depend on the dielectric permittivity ϵ and geometrical parameter described in eq.1 [38]. The electric resonant response arises from the charge displacement that happens when the incoming light couples efficiently in one of the electric multipoles, while the magnetic response is the result of circulating displacement currents of the electric field. These magnetic resonances can be excited in non-magnetic dielectrics because high refractive index materials induce significant phase retardation and field penetration, allowing the electric field to form the closed loops required for generating magnetic dipole moments. The radiation patterns of the lowest-order resonant modes are shown in Fig. 5.

Different shapes and geometries of dielectric meta-atoms are possible, and by tuning these parameters, the resonant response of the metasurface can be tuned to overlap the magnetic and electric multipoles excitations. This spectral overlapping can lead to interference or coupling between a few or several multipole modes, giving rise to more complex resonant features and more degrees of freedom to manipulate the incoming light properties. The main scattering phenomena observed in dielectric metasurfaces will be explained below.

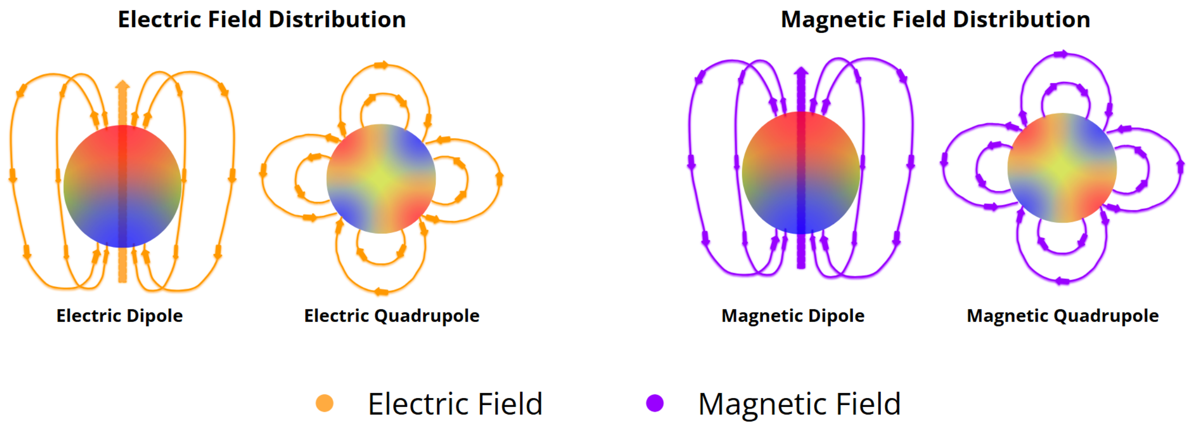

Figure 5: Electric and Magnetic field distributions and radiation patterns for the four lowest-order Mie resonant modes inside a sphere.

Kerker Effect

The dielectric metasurfaces' capability of simultaneously supporting electric and magnetic multipoles resonances enables strong directional scattering of the incoming light. In fact, by using the formulation of Mie theory in eq. 2, it was demonstrated that when $a_1 = b_1$, which corresponds to the electric and magnetic dipoles, the metasurface could exhibit no backward scattering. This holds true provided that the higher-order coefficients are small enough to be ignored[39]. This condition, known as the first Kerker condition, requires the two dipoles to oscillate in phase at the origin. On the other hand, when $a_1 = -b_1$, and there is a $\pm\pi$ phase shift between the interfering dipoles, destructive interference will happen in the forward direction. This is referred to as the second Kerker condition, and it results in suppression of forward scattering. Each dipole can impart a maximum π phase shift to the incoming light by supporting both in the same structure. Full phase control can be achieved with close to unity transmission when the first Kerker condition is satisfied. This property has enabled the design of so-called *Huygens Metasurfaces*, in which each scatterer acts as a Huygens source, but radiating in the forward direction only. Before the arrival of dielectric resonant metasurfaces, this concept had been first tested by using plasmonics, but the inherent losses and the lack of full-phase coverage limited the capabilities of these devices[40].

Fano Resonances

Other scattering phenomena that appear when different multipoles are simultaneously excited are Fano resonances. This type of resonances are due to the interference of a broad and narrow resonance in the same physical system, and as such, they appear across a wide range of platforms ranging from photonic crystals and plasmonic structures to atomic and molecular physics and superconductors. In metasurfaces, their appearance originates from Mie scattering where a narrow resonance such as those supported by electric or magnetic quadrupoles, interferes with a spectrally broader one, which is typically a dipole resonance. The scattering cross section for a Fano resonance has a characteristic asymmetric lineshape described by the formula[10]:

$$\sigma(E) = D^2 \frac{(q+\Omega)^2}{1+\Omega^2} \tag{3}$$

where q is the Fano parameter, $\Omega = \frac{2(E-E_0)}{\Gamma}$, Γ is the resonance width and E_0 is the resonance energy. The formula is not limited to the description of the scattering cross section, but can also be used to describe the transmission, absorption or reflection spectra. A Fano resonance can be modelled by two coupled driven oscillators with different damping rates[41]. While the undamped oscillator imparts a π phase shift at the resonance, the phase of the strongly damped oscillator varies slowly, resulting in the typical asymmetric shape shown in Fig. 6

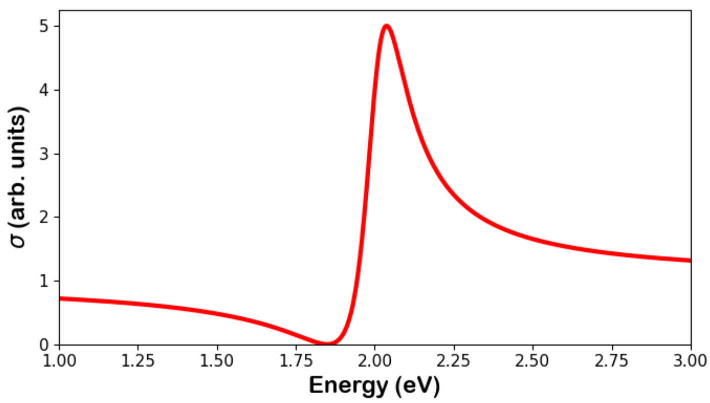

Figure 6: Scattering cross section with an asymmetric Fano shape.

Bound States in the Continuum

Bound States in the Continuum (BICs) are resonances associated with very high Q-factors. These states were first mathematically discovered in 1929 in the field of quantum mechanics[42], but they are a phenomenon emerging from the wave description of physical systems, and as such, they can be found in acoustics, fluid dynamics and photonics. They are an exception to the most common situation, in which a resonant system coupled to external continuous states will inevitably lose its energy over time by radiating into a number of these states. In a BIC, the energy is completely spatially localized in the resonator, even if the system could support propagation through the continuous modes[43]. BICs can be found in many physical systems because they originate from destructive wave interference. In metasurfaces for example, the periodicity of the structure allows the coupling of the modes to the continuum, typically turning them into leaky resonances. At the same time however, the patterned surface causes light to backscatter. If the metasurface is highly symmetric, specific resonant mode symmetries could originate and interfere destructively or constructively. In a so called *symmetry protected BIC*, the mode's profile causes the destructive interference of light, creating non-leaky resonance that is incompatible with the radiation channel symmetry, effectively trapping the light. At nonzero wavevectors, i.e. at oblique incidence of light, coupling to the radiation channel can disappear when the multipole profiles of the mode destructively interfere. This type of BICs, called *accidental BICs*, are not guaranteed by symmetry alone like in the previous case, but require fine tuning of the meta-atoms geometric parameters. Pure BICs exist only as mathematical objects with infinite Q-factors. Nevertheless, they manifest in the real world as *quasi-BICs*, which are leaky resonant modes obtained by breaking the structural symmetry of the metasurfaces or by tuning the geometrical parameters. Despite the leakage to the continuum, quasi-BICs posses high Q-factors and can achieve significant field enhancement inside the scatterers. Originating from the same interference mechanism between broad and sharp modes, Quasi-BICs are a type of Fano resonance, and as such they manifest themselves in the far-field spectrum as Fano lineshapes with high Q-factors.

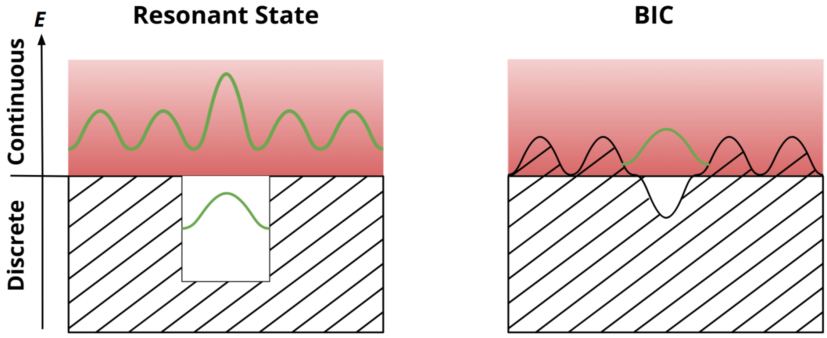

Figure 7: A particle inside a potential well can be described by a set of localized states with discrete energies and propagating waves with continuous energy values. A resonant state necessarily includes components lying within the continuum, letting the state propagate outside the well and exhibit a nonzero spectral linewidth. A BIC behaves like a state with discrete energies residing within the continuum, with the non-leaking and localized state resulting from the destructive interference between the continuum components. Illustration adapted from[43].

2.2.1 Lattice Resonances

Lattice resonances arise from the collective resonant response in the individual meta-atoms and are therefore inherently nonlocal in nature. In particular, it is possible to distinguish one class of these resonances called *surface lattice resonances* (SLRs). They originate from the enhanced coupling between the individual meta-atoms' resonances that happens when the diffraction orders propagate along the metasurface. These diffraction orders begin to propagate on the surface when they switch from being evanescent waves to grazing waves, a condition known as *Rayleigh Anomaly*, occuring when $\Lambda \approx \lambda$. These types of in-plane diffraction orders allow the meta-atoms to "connect" with their neighbours over the length of the metasurfaces[44], generating collective resonant effects. The wavelength λ_{RA} at which a Rayleigh anomaly appears depends on the refractive index of the embedding medium and the substrate in use. In Ref. [45] for example, it is discussed how a metasurface with a periodicity of 485 nm produces an RA at 613 nm due to the use of silica as the embedding medium.

2.3 Nonlinear Optics

The direct interaction between photons are intrinsically weak, but already after the invention of the first laser in 1960, it became clear that photon-photon interactions could emerge for sufficiently high light intensity. Usually, when light is incident on a material, the collective motion of electrons radiate light that scales linearly with the incoming radiation, but when the incident field amplitude is large enough, the polarization density $\vec{P}$ of the material starts to become non-parallel to the electric field. Under these conditions, the optical response of the material becomes intensity dependent and nonlinear with respect to the incoming field.

A variety of new and fascinating optical effects are possible in the field of nonlinear optics, all sharing the common feature that the nonlinearity emerge as light interaction mediated by the materials in use. This section focuses on the nonlinear interactions most relevant to the present work, along with a brief overview of recent achievements in the field of metasurfaces in nonlinear optics.

2.3.1 Second and Third Harmonic Generation

When considering a linear dielectric material, the medium polarization P relation to the applied electric field E can be expressed as:

$$P = \epsilon_0 \chi^{(1)} E \tag{4}$$

Where $\chi^{(1)}$ is the linear susceptibility of the material. However, this linear behaviour is just an approximation, as demonstrated by Peter Franken in 1961 [46], and a better formulation of equation 4 can be written by expanding the function in a Taylor series:

$$P = \epsilon_0 (\chi^{(1)} E + \chi^{(2)} E^2 + \chi^{(1)} E \chi^{(3)} E^3 + ...) \tag{5}$$

This non-linear interaction generates new frequencies in the scattered optical field. For example, if an input wave with an electric field $E \propto \exp[i\omega t]$ enters the medium, a second order polarization component $P^{(2)} \propto \chi^{(2)} \exp[-2i\omega t]$ will be generated, oscillating with a doubled frequency.

Nevertheless, while second-order nonlinear interaction can still be observed at low intensities, it starts to be significant when the input electric field approaches the typical intra-atomic field strength of 10^{11} V/m, which is within reach of laser sources, and occurs only when anisotropic media are used, i.e. media with $\chi^{(2)} \neq 0$[47].
Eq.5 shows that the P also posses a term oscillating at 3ω, in this case the medium responds to the optical field by generating light at a tripled frequency.

These processes can be viewed as an interaction between two or three photons respectively, in which the annihilation of incoming photons oscillating at the fundamental frequency ω_1 generates a photon with a frequency ω_2, which is double or triple ω_1. These newly generated fields oscillating at multiples of the fundamental frequency are called *harmonics*, and the two processes described earlier are consequently named *second and third harmonic generation* or SHG and THG.

Nonetheless, the generation of these new frequencies can only happen when certain conditions are met. Using the photon picture and considering the SHG process, the input and output photons must follow the energy conservation law:

$$\hbar\omega_1 + \hbar\omega_1 = \hbar\omega_2 \tag{6}$$

as well as the momentum conservation law:

$$\hbar\vec{k_1} + \hbar\vec{k_1} = \hbar\vec{k_2} \tag{7}$$

Eq.7 is referred to as *Phase Matching Condition* and in the wave picture it describes the matching between the wavefronts of the frequencies involved. It is possible to demonstrate that when the quantity $\Delta k = k_1 + k_1 - k_3 = 0$, the generated wave can receive energy from the incoming waves with the highest efficiency [48]. For a collinear process, eq.7 translates into a scalar equation:

$$\frac{n_1\omega_1}{c_0} + \frac{n_1\omega_1}{c_0} = \frac{n_2\omega_2}{c_0} \tag{8}$$

That would be impossible to solve due to the different refractive indices that the material exhibits due to dispersion. Because of this, second-order nonlinear optical effects are usually generated by the use of anisotropic media, where the refractive index have different values depending on which axis the polarization of the incoming light is oriented. By tuning the light incident angle at the medium and the light polarization, it is then possible to satisfy eq. 8, obtaining $n_1 = n_2$.

Nevertheless, a slight phase-mismatch Δk is still possible, which corresponds to a maximum length called *coherence length*, in which the nonlinear processes are still efficient[48]:

$$L_c = 2\pi/|\Delta k| \tag{9}$$

In general, nonlinear phenomena are subject to symmetry requirements, imposing a physical limit on the type of materials that can be used. For example, centrosymmetric materials possess inversion symmetry and the material's optical properties are not altered by a transformation $r \to -r$, it is evident from eq.5 that the odd symmetry of P is not respected by the parity of E^2. Because of this, in centrosymmetric and amorphous materials $\chi^{(2)} = 0$, leaving the third order as the lowest permitted nonlinear contribution.

While being weaker, third order nonlinear effects are not bound by this constraint because the odd symmetry is respected for both P and E, and can be observed in virtually every material.

2.3.2 White Light Generation

Another important non-linear phenomenon that will be used to measure the resonant response of the metasurfaces is *White Light Generation*. It consists of the broadening of the pulse spectrum into a white light continuum, known as supercontinuum [49].

Light propagating inside a Kerr medium, i.e. a medium with $\chi^{(3)}$ exhibiting a third-order nonlinear response, will be subjected to a different refractive index depending on its local intensity. In particular, a Kerr medium is characterized by a refractive index $n = n_0 + n_2 I$ with n_0 being the linear refractive index, n_2 the non-linear refractive index and I being the intensity[48].

This effect can give rise to self-phase modulation(SPM), in which light propagating inside a third-order non-linear medium undergoes a phase shift $\Delta\varphi$ defined as [48]:

$$\Delta\varphi(t) = -2n_2 \frac{L}{\lambda_0 A} P(t) \tag{10}$$

Where $P(t)$ is the optical power, A is the cross-sectional area and L is the distance.
The introduced time-dependent phase causes a variation of the instantaneous pulse frequency $\omega(t)$, defined as [50]:

$$\omega(t) = \omega_0 + \Delta\omega(t) \tag{11}$$

with:

$$\Delta\omega(t) = \frac{d\Delta\varphi(t)}{dt} \tag{12}$$

If self-phase modulation happens to be very strong, $\Delta\omega$ could exceed the original spectral width of the pulse, generating light with a wide spectrum.

3 Methods

The methods employed in this thesis to design, fabricate and characterize the dielectric resonant metasurfaces will be described in this chapter. The first part will present the finite element method (FEM), its implementation in COMSOL and the simulation methodology adopted to study the meta-atom scattering response and the metasurface resonances. The second part will cover the fabrication processes that were involved in fabricating the metasurfaces from the substrate to the final device. The third part will illustrate the white light spectroscopy setup used to characterize the fabricated metasurfaces.

3.1 Simulations

This section describes the main workflow for performing simulations in COMSOL using the Wave Optics module. The first subsection will briefly explain the finite element method, while the second part covers the general setup that is common to all simulations performed in this thesis, including the definition of the geometry, material properties and meshing. The third subsection focuses more on the meta-atom simulations used to identify the supported Mie resonances in a single scatterer, with a brief discussion on the multipole decomposition. The final subsection describes the metasurface simulations where periodic boundary conditions are used to compute the transmission, reflection and phase response of the infinite array of meta-atoms.

3.1.1 Finite Element Method (FEM) and the Weak Formulation

COMSOL Multiphysics was used to simulate the electromagnetic response of the structures. Based on the FEM as its core numerical framework, COMSOL is a general-purpose finite element analysis (FEA) simulation software. Here, a brief overview of the FEM will be given, with particular emphasis on its application for electromagnetic simulations.

The laws of physics are usually expressed in terms of partial differential equations (PDEs), for this reason multiphysics simulations software like COMSOL, can be viewed as solvers of approximated PDEs. The approximated equations are needed because for the majority of problems, the PDEs cannot be solved analytically, and numerical models need to be used. The purpose of FEM is to transform the equations into numerical equations and compute their solutions to reach an approximated result of the corresponding PDEs.

To modify a PDE to be a numerical equation the so called *weak formulation* is employed, which turns the differential formulation into an integral equation. For example, considering the Laplace equation for electrostatics in 1D

$$\frac{d}{dx}(\frac{dV}{dx}) = 0 \tag{13}$$

the solution to this equation gives the value of the potential V at the x locations within the domain. Ultimately, because the electric field $E(x) = -\frac{dV}{dx}$, the desired equation to solve is:

$$\frac{dE}{dx} = 0 \tag{14}$$

Both these two equations are not numerically solvable for every geometry or situation. To solve them numerically, one has to transform them into integral equations. Considering a domain restricted between 0 and 1 for example, the value of eq. 14 at $x = 0.5$ can be approximated by:

$$\int_{0.49}^{0.51} \frac{dE}{dx} dx \tag{15}$$

By extending this idea to every domain location, one can restore the solution of the PDE by solving a series of equations like eq. 15. This sampling of the function can be done by using a set of so called *test functions* $T(x)$ that are not negligible only for a narrow range as illustrated in Fig.8:

$$\int_{0}^{1} \frac{dE}{dx} T(x) dx = 0 \tag{16}$$

This integration step is then followed by integration by parts to reduce the order of differentiation:

$$\int_{0}^{1} E(x) \frac{dT}{dx} dx = +E(1)T(1) - E(0)T(0) \tag{17}$$

With the boundary conditions on the right hand of the equations being unique for every problem. To obtain a good approximation of the solution, one has to solve the weak equation for a finite number of test functions, resulting in a finite number of equations to solve.

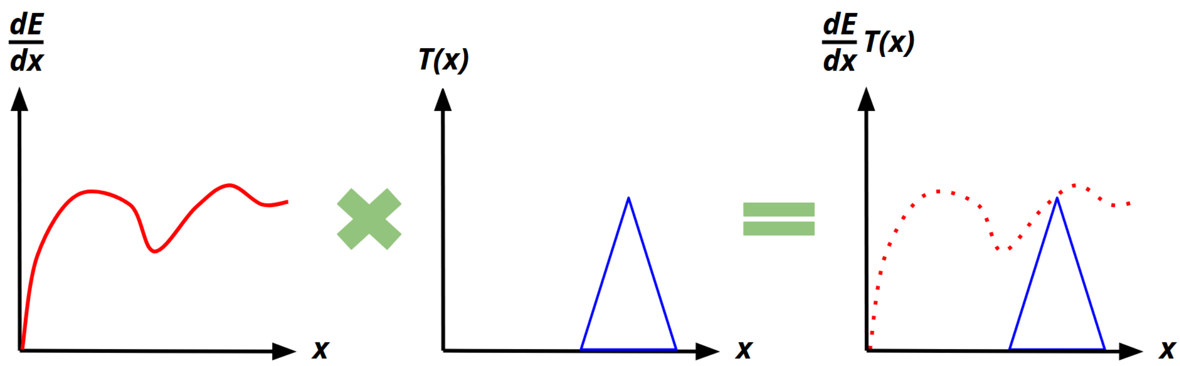

Figure 8: Schematic of the weak formulation principle. A derivative is multiplied by a localized test function T(x), effectively sampling the function over a subdomain.

A simulation study in COMSOL requires the user to divide the geometry of the problem into smaller elements, in a practice called *meshing*. The test functions on each element, often polynomials, can then be defined such that they are non-zero only for a small group of neighbours. Meshing ultimately decides how refined the simulation will be, a finer mesh will produce a more accurate solution due to more test functions involved. COMSOL uses the so called *Ritz-Galerkin* method[51] to obtain an approximated solution to the problem that is represented by a superposition of all the test functions used for the simulation.

In synthesis, FEM approximate the function $E(x)$ using a linear combination of simpler functions $\psi_i(x)$ such that:

$$E(x) \approx \sum_i c_i \psi_i(x) \tag{18}$$

where c_i indicate the weight coefficients of ψ_i. The illustration in Fig. 9 depicts an example of this approximation method.

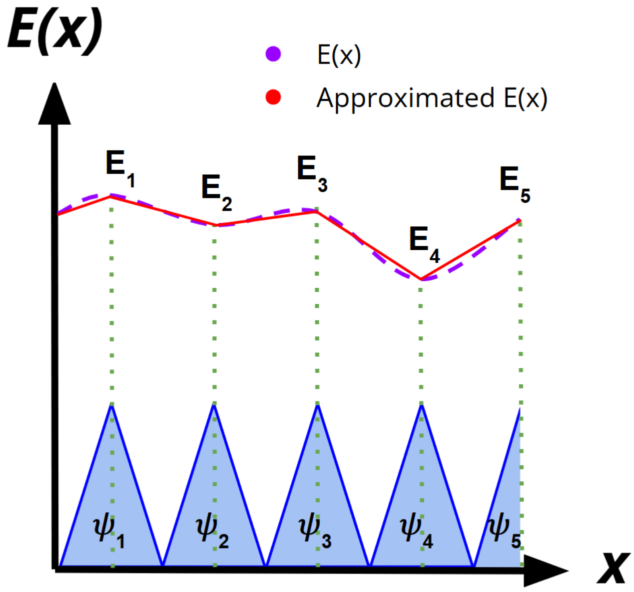

Figure 9: Schematic of the approximation method employed by the FEM. The function is approximated as a linear combination of simple functions ψ_i.

The 1D example discussed here is simple, but the procedure and the idea behind the FEM stays the same even for higher dimensions equations.

For electromagnetics simulations, COMSOL solves the Maxwell's equations in 3D under the assumption that the fields vary sinusoidally at $\omega = 2\pi f$, and that the material's properties are linear with respect to the field:

$$\nabla \times (\mu^{-1} \nabla \times \vec{E}) - \frac{\omega^2}{c_0^2}(\epsilon_r - \frac{i\sigma}{\omega\epsilon_0})\vec{E} = 0 \tag{19}$$

The solution of this equation returns the electric field profile $\vec{E}(x, y, z)$ through the domain. The other important quantities such as magnetic field, power, current ecc. can all be derived from the solution for the electric field.

The great advantage of FEM is that it is possible to choose the amount of discretisation for the domain and the shape of the test functions. In fact, while PDEs like eq.19 can become an issue for non-smooth surfaces, gradients or physical effects, the weak formulation transforms the equations into integrals, which can then be calculated over the mesh elements.

3.1.2 Simulations Workflow

To simulate the electromagnetic response of objects, COMSOL has a built-in editor where simple shapes and geometries can be initialized to define the simulation volume. For this thesis, the two main geometrical shapes will be cylinders, for the creation of the meta-atom pillars, and rectangular blocks, to define the air column in which the pillars are located. Usually, all geometrical dimensions, like the pillar's diameter and height for example, are defined as global parameters instead of fixed values in the geometry tab. This allows parametric sweeps over these quantities automatically during the simulation, instead of modifying the geometry manually every time.

After setting up the geometry with the correct parameters, each object needs to be assigned to a material. While it is possible to create and customise a material manually, COMSOL offers several built-in material data sets for dielectric materials, so the simulations performed in this thesis will be mainly based on existing data. Each material properties of interest for the chosen module are listed under the Material Contents section, and can be modified if needed. These material properties allow COMSOL to obtain the parameters to numerically solve the PDEs through the FEM method.

When all the objects and their materials are defined, the next step is to define the physics. For metasurface and meta-atoms simulations, the Electromagnetic Waves, frequency domain interface was used throughout the thesis. Defining the physics means assigning each object to mathematical equations dependent on the type of simulation to be performed. Within this interface, it is possible to initialize the source type, the polarization and the angle of incidence of the incoming light. In this work, a plane wave was used as the excitation source with normal incidence and linear polarization in the x-direction. Additionally, the interface allows to specify the boundary conditions applied to every object in the simulation domain, which determines how the electromagnetic fields behave at the edges of each volume.

In this thesis, every component in the simulation domain was assigned to eq.19 except for particular regions called *Perfectly Matched Layers* or PMLs. PMLs are artificial regions placed at the boundaries of the simulation domain designed to absorb the incoming light with minimum reflections. PMLs gradually attenuate the fields making the transition from the physical domain to the boundary reflectionless regardless of the incoming wave type. Without PMLs the light would reflect back into the physical domain, invalidating all simulation results.

As previously mentioned, the FEM method divides the simulation region by using polygons in a practice called *meshing*. COMSOL offers great customizability over the mesh size, but it can also automatically choose the proper mesh depending on a geometric analysis of the components and the physics interface in use. Using this feature, COMSOL offers 9 different choices of element sizes, from extremely fine to extremely coarse. While the mesh size needs to be small enough to accurately solve the field variations at curved interfaces, meshing greatly affects the computational time, for this reason, the simulations performed in this thesis used a mesh of only fine or finer element sizes to achieve a good compromise between accuracy and speed. A good rule of thumb is to choose a mesh with elements having a maximum size of a fraction of λ/n inside each material, which means that the high-index pillars require a finer mesh compared to air or the substrate for example.

The final procedure after meshing is to run the simulation. In this step, a wavelength sweep could be implemented, together with a parametric sweep, where one or more parameters like the pillar's radius and height can be modified continuously to observe the changes in the electromagnetic response. The solver computes the fields at each wavelength independently, and the results are then post-processed to extract transmission, phase shift and reflection spectra as well as other relevant information.

All the simulations were performed using the LUNARC High-Performance-Computing (HPC) center provided by Lund University, running on a single node of two AMD EPYC 7413 Milan CPUs with 24 cores each and with an available memory of 257 GB. LUNARC uses the Simple Linux Utility for Resource Management (SLURM) to manage the programs that need to be executed. For this reason a SLURM file, containing the instructions and requirements needed to perform the COMSOL simulations on the HPC cluster, was created and run for each simulation. The output files containing the results were then transferred from the HPC to the local computer using the file manager WinSCP.

3.1.3 Simulation of the meta-atoms scattering response

To simulate the scattering response of single meta-atoms and observe which Mie-resonances are supported within the pillars, the simulations were performed using a single element surrounded by air and a PML layer. In the Electromagnetic Waves, frequency domain settings the formulation was changed from full-field to scattered field, which means that solving eq.19 for $E_{tot} = E_b + E_{relative}$ where E_b is known and representing the background source term, eventually return the solution for $E_{relative}$, which indicates the scattered field from the meta-atom. COMSOL lets the user choose the background wave type as well as the polarization and the amplitude. A cross section calculation was also added to the domain by selecting the meta-atom pillar.

The simulation domain for the single meta-atom study consisted of three concentric structures: the pillar, an air sphere with a 900 nm radius to let the electric field propagate for a distance of at least one complete wavelength, and a surrounding PML layer 900 nm thick to absorb the scattered radiation. The mesh was set to fine. The source consisted of an x polarized plane wave having a 1 V/m amplitude and with a spectrum ranging from 400 nm to 900 nm. A snapshot of the simulation domain from COMSOL is shown in Fig. 10.

While the simulation results gave information about the field distributions inside the pillar and the total scattering cross section, the contribution of each resonant mode could not be obtained by only using COMSOL. In fact, commercially available software for simulating electromagnetic phenomena, including COMSOL, don't provide a straightforward built-in method to achieve this decomposition. For this reason, a method called *multipole decomposition* or *multipole expansion* was performed by post-processing the results from the simulations.

The multipole expansion is based on the decomposition of the radiation emitted from arbitrary charge and current distributions into contributions from each multipole order. Fundamentally, it is the same procedure as seen in eq. 2 for the Mie-theory of scattering, but while Mie exploited the spherical symmetry of the problem to find an analytical solution, the multipole expansion is more general and can be applied to arbitrary source distributions [52].

In this thesis, the multipole expansion was performed through an open-source MATLAB code called *Multipole Expansion for NanoPhotonics* (MENP), which is available and described in [53]. MENP calculates the induced current density distributions $\vec{J}(\vec{r})$, obtained from the electric field distributions $\vec{E}(\vec{r})$ by using the expression:

$$\vec{J}(\vec{r}) = -i\omega\epsilon_0(n^2 - 1)\vec{E}(\vec{r}) \tag{20}$$

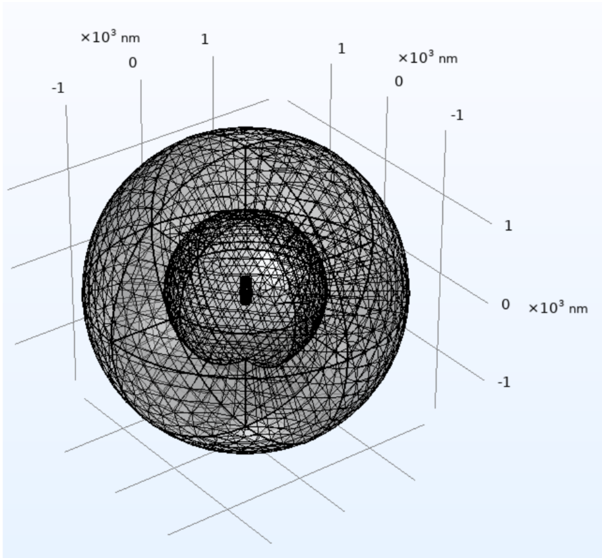

Figure 10: Simulation domain for studying the scattering response of meta-atom pillars in COMSOL.

The current density is then used to calculate the multipole moments and their relative scattering cross section up to the quadrupole order. In order to do these calculations, the method required as inputs two 4D matrices: the electric field distribution $\vec{E}(x, y, z, \lambda)$ and the refractive index distribution $n(x, y, z, \lambda)$. For every parameter change, both data were exported after completing the simulation, transformed into a MATLAB file and used to compute the total scattering cross section and each multipole contribution.

3.1.4 Simulation of the metasurfaces resonant response

Following the single meta-atom study, the focus was placed on simulating the resonant response of metasurfaces. Since the release of COMSOL 6.3, the method to simulate periodic structures like metasurfaces has been greatly simplified. The modelling requires the definition of a unit cell that will then be infinitely repeated in two dimensions, with each pair of parallel boundaries getting assigned to Floquet Periodic conditions as boundary conditions. Version 6.3 introduced the Periodic structure node to the Wave Optics module, which can be assigned to the objects that compose the unit cell. This selection automatically adds the required excitation and output ports, which indicate the interface at which the incoming light is inserted and absorbed, respectively. Additionally, it is possible to choose the incoming wave type from the port settings, as well as its polarization, angle of incidence and azimuthal angle.

The metasurface studies were carried out by embedding the pillars in a 2.5 μm tall air domain, bounded at the top and bottom by PML layers to ensure that no reflected light from the ports could reflect back into the simulation domain. The structures developed along the z direction, which correspond to the propagation direction of the source. The excitation port was placed at the bottom of the air domain, at the interface with the lower PML. Periodic boundary conditions were automatically applied to the lateral faces of the simulation domain to replicate the metasurface periodicity. The x and y dimensions of the unit cell were set equal to the desired lattice constant, since in a periodic simulation the lateral size of the domain directly corresponds to the center-to-center distance between pillars. Equal side lengths were chosen in both directions to keep the design symmetric and ensure a fair comparison across the different metasurface configurations. A picture of the simulation domain from COMSOL for the metasurface's simulation is shown in Fig. 11.

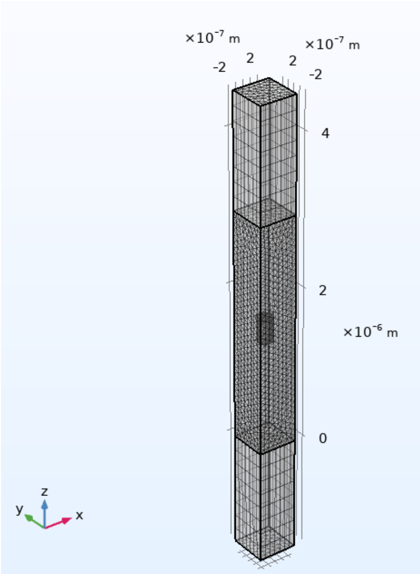

Figure 11: Simulation domain for studying the scattering response of the metasurfaces in COMSOL.

3.2 Fabrication

The fabrication accuracy is crucial for experimentally validating the resonant behaviour predicted by simulations. This section describes the fabrication methods employed to realise two metasurface designs, along with a brief introduction to each tool used throughout the process. The two designs were chosen based on the resonant study of the geometrical parameters presented later in section 4.1 and consist of equally spaced TiO_2 meta-atoms, arranged with a periodicity $P = 500$ nm, a height $H = 300$ nm and with pillar diameters of $D = 140$ nm and 145 nm respectively. All of the following processes were carried out in the cleanroom at Lund NanoLab(LNL) under the supervision of Jeevan Rois, PhD student in the research group where this thesis was performed.

Sample preparation

Because the two simulated metasurfaces were designed to work in transmission and in the visible spectral range, a 500 μm thick fused silica wafer was chosen as the substrate due to its transparency. The SiO_2 wafer was first cleaned by placing it in a beaker with acetone. After an ultrasonic bath of 3 minutes, the wafer was placed in another beaker containing IPA and the ultrasonic bath was repeated. A dehydration bake was then performed by placing the wafer on a hot plate at 150° for about 5 minutes. The AR-P 6200.13 positive resist was spin coated on the cleaned wafer to obtain a layer thickness of around 300 nm. This step was followed by baking on a hot plate at 150° for 8 minutes. A 40 nm thick AR-PC 5002.02 conductive layer was then spin coated on top of the resist, followed by another bake at 90° for 2 minutes.

Patterning
Electron beam lithography (EBL) was used to pattern the metasurfaces. Unlike optical lithography, EBL writes patterns by scanning a focused electron beam directly on the resist. This process does not require a physical mask, which makes it highly convenient for research applications where design flexibility and fast prototyping have priority over the high throughput of optical lithography. The main limitation of EBL is its relatively slow writing speeds compared to optical lithography, which makes it inefficient for patterning over large areas. The patterning was performed using an EBL Voyager from Raith, the electron acceleration voltage was set to 50 KeV, and after a dose test, a suitable dose of 190 μC/cm^2 was found to achieve the correct pillar resolution. The patterning file was designed so that the electron beam could expose the positive resist only at the pillar locations. The relatively low density, combined with the pillar's small dimensions, helped achieve the correct feature size while keeping the writing time to 4 hours. The two patterns had a device area of 1×1 mm^2 and 0.5×0.5 mm^2 respectively, with a distance between them of around 0.5 mm.

Development
The patterned chip was placed in a beaker with water for 45 seconds to remove the top conductive layer, followed by a bath in amyl acetate for 1 minute to remove the exposed resist and create the cavities where the pillars would be built.

Atomic Layer Deposition
Atomic Layer Deposition (ALD) was used to conformally fill the cavities to create the pillar structure of the metasurfaces. ALD is a thin-film deposition technique based on sequential, self-limiting surface reactions between some gaseous precursors and the substrate. Because each precursor cycle and its purge happen sequentially, the film can grow one atomic layer at a time, giving precise control over the material thickness. This high degree of control and the good conformality of the deposited material make ALD well suited for filling the cavities to create the pillars. To prevent material deposition under the sample due to the tool area not being completely flat, the chip was placed on a silicon substrate and secured to it using some tape. A picture of the patterned sample on the wafer is shown in Fig. 12. An ALD Fiji from Cambridge Nanotech was used to deposit TiO_2 onto the patterned surface. The recipe consisted of a 0.5 s precursor pulse, a pause for 15 s, activation of plasma at a power of 300 W for 5 s, and a pause of 15 s before the purge. This cycle was repeated 2300 times to completely fill the cavities on the surface.

Etching
Inductively coupled plasma reactive ion etching (ICP-RIE) was used to remove the layer of TiO_2 that was deposited on top of the metasurface to fill the pillar cavities. ICP-RIE is a dry etching technique that combines chemical reactions with physical ion bombardment to remove the ma-

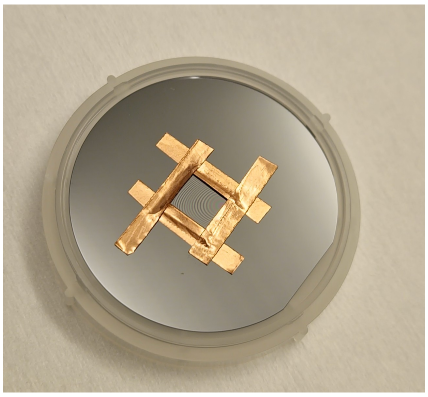

Figure 12: Picture of the patterned sample secured to the silicon wafer with a tape before getting placed in the ALD chamber.

terial. Compared to conventional RIE, the coupled plasma source generates a denser plasma, allowing the ion energy and plasma density to be controlled independently, resulting in higher etch rates. A ICP-RIE APEX SLR from Advanced Vacuum Systems AB, using fluorine-based chemistry and an RF power of 30 W, was used to etch the deposited TiO_2 on top of the pillars. First, using an ellipsometer, a TiO_2 thickness of 51 nm was measured on the silicon wafer used as the ALD platform for the chip. Then, a 1 minute etching was performed using the same wafer to calculate the etch rate of the tool. The second ellipsometry measurement after this etch test resulted in a TiO_2 thickness of 16.55 nm, resulting in an etch rate of 34.5 nm/ min. Knowing this and the 51 nm TiO_2 residual layer thickness on the sample, etching was performed for about 90 seconds to completely remove the unwanted material. The resist between pillars was then removed by O_2 plasma ashing for 5 minutes, while the remaining residual resist was removed by placing the chip in a remover 1165 bath for 40 minutes at 80°. An illustration of all the involved processes for the metasurface's fabrication is depicted in Fig. 14. The result for the $0.5\times$ 0.5 mm^2 metasurface after etching and development under the optical microscope can be seen in Fig. 13.

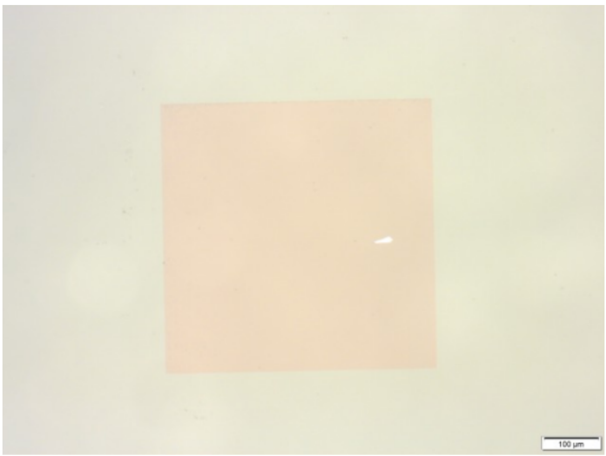

Figure 13: Picture under the optical microscope of the 0.5×0.5 mm^2 metasurface after fabrication.

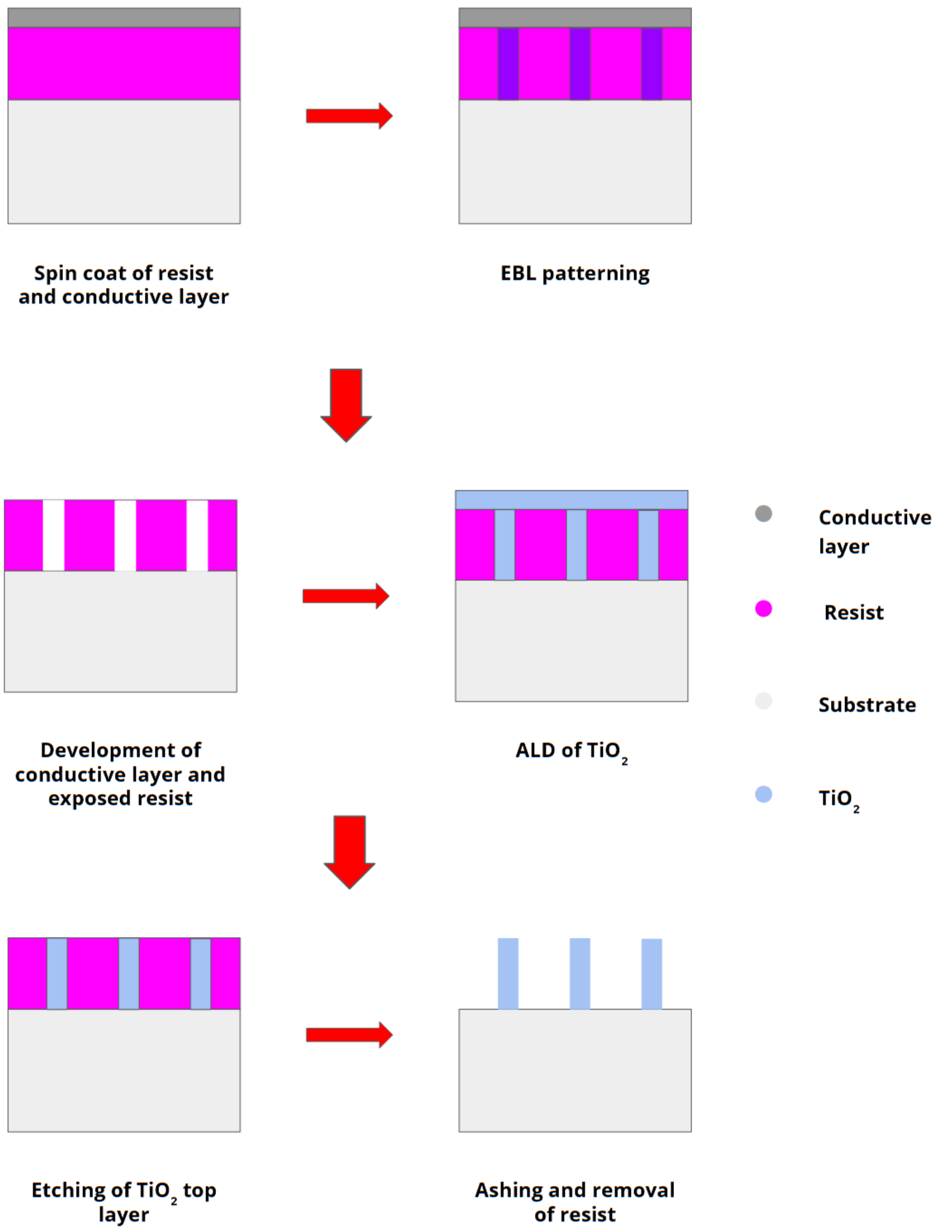

Figure 14: Schematic illustration of the metasurface fabrication processes. The conductive layer is shown in dark grey, the resist in pink, the fused silica substrate in light grey, while the light blue material is TiO_2.

3.3 White Light Spectroscopy

To measure the transmission spectra of the two fabricated metasurfaces, an interferometer was built on an optical bench. While the entirety of the interferometer was not needed for measuring only the transmission spectra, the interferometer was built for future phase characterizations of resonant metasurfaces. In this work, the phase response was not characterized as the results from the transmission measurements suggested the need for further optimizations of the measurement setup to obtain a meaningful phase study. The time constraints did not allow for this within the scope of this thesis. The experimental setup together with pictures of the illuminated metasurfaces is illustrated in Fig. 15. It uses a white-light laser WL as the source, which is well suited for the resonance study given its broad spectral coverage. Before the first reflection at mirror M1, a bandpass filter F was placed in front of the beam to select the light within the 400-600 nm spectral range. A second mirror M2 was then placed and tuned to steer the reflected beam toward the interferometer. An aperture A1 placed before the first beam splitter BM1 reduces the beam diameter to match the size of the metasurfaces. At BM1, the beam is split into two, with one beam going through the metasurface chip S, bouncing off mirrors M3 and M4 before reaching the second beam splitter BM2. Part of the incoming beam after A1 reflects off BM1 to form the second arm of the interferometer. This beam, propagating perpendicularly compared to the incoming beam, then reaches a phase delay stage PD composed of two identical oblique small mirrors, which redirect the light towards mirror M5. After reflecting off M5, the beam reaches BM2, where its reflection is then recollimated with the reflected beam coming from M4. Then, the single beam from BM2 passes through a second aperture A2 before reaching the fiber coupler FC, which collects the light into a multi-mode fiber connected to a spectrometer at the other end of the fiber. The position the metasurfaces accurately, the chip was mounted between two clamping plates screwed onto a holder. The holder was fixed to a movable stage which was aligned to have the beam impinging along the axis connecting the two metasurfaces, allowing the switch between them to be controlled by only tuning the height of the stage.

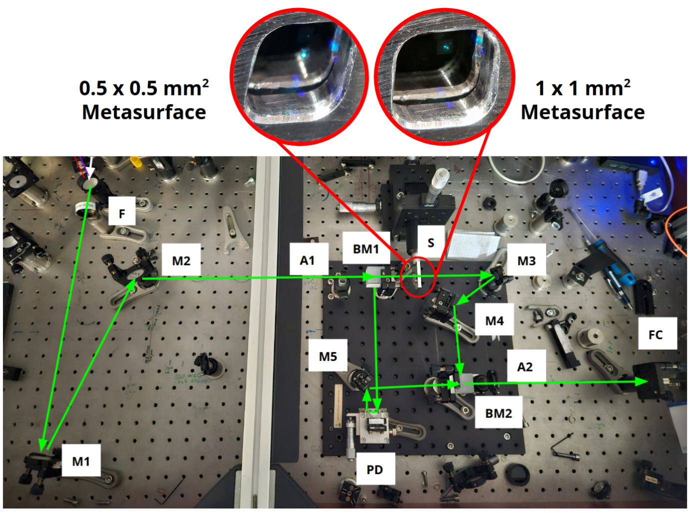

Figure 15: Picture of the white light interferometer with illustration of the beam path. An inset showing pictures of the two illuminated metasurfaces on the same chip (S) is shown.

4 Results and Discussion

This chapter will describe the results of the simulations and the experimental characterization of dielectric resonant metasurfaces in the visible spectrum.

The first section will be focused on the study of resonant metasurfaces with a core-shell structure. The goal was to explore the resonant behaviour of metasurfaces when more than one dielectric material has been used for fabricating the meta-atoms. The two materials of choice in this part were TiO_2 and HfO_2. As described in chapter 1, the transparency and high refractive index in the visible range make both dielectric materials suitable candidates for exploring the core-shell structure and resonant mechanisms in metasurfaces in the visible range.

Firstly, the scattering response of single meta-atoms was investigated to show which type of Mie-resonances were possible to excite. Meta-atoms with core-shell structures are then examined to see the differences in the scattering response compared to the monolithic meta-atoms. The scattering contribution of each multipole is obtained through the multipole decomposition method, while the simulations were performed in COMSOL Multiphysics.

After, the resonant effects of dielectric metasurfaces were studied by simulating their transmission, reflection and phase responses. A similar comparison was carried out between TiO_2/HfO_2 metasurfaces, core-shell metasurfaces and effective material metasurfaces, where the refractive index of the latter was modelled to replicate the composition of core-shell metasurfaces. The simulation study shows how the geometrical parameters of the meta-atoms, as well as the periodicity of the lattice, change the resonant response. Moreover, two metasurface designs were chosen to validate the simulation results and to observe the resonances. The metasurfaces fabrication was carried out at LNL as described in section 3.2 and their transmission spectra were then observed by placing them in one arm of an interferometer as described in section 3.3.

The second part will be dedicated to a conceptional design of a metasurface for harmonic generation. The concept has been developed with the intent of placing the metasurface inside a multi-pass cell (MPC), where the incoming light is generated by an ultrafast laser source with a bandwidth of 10 nm centered at 1030 nm and a pulse duration of around 180 fs. It has to be noted that this part of the project involved only the design process, while the fabrication and the metasurface testing for this application would require further work and are left as a prospect for future investigations.

The resonant response and the harmonic order generated by the metasurface are dependent on the material and the geometrical parameters, so both these aspects were investigated to choose a suitable design correctly. COMSOL is not suitable for studying harmonic generation due to the lack of a nonlinear optics module and physics, and simulating a nonlinear response from structures in the software is not trivial and could become time consuming because the user would have to implement the coupling of the fundamental and the higher harmonics using one additional physics interface and manually add nonlinear polarization terms. In this thesis, the main figure of merit for choosing a suitable device has been the electric and magnetic field enhancement inside the structures, which is the driving force behind harmonic generation using metasurfaces. This approach can still indicate good choices for design parameters, even if the nonlinear response cannot be measured quantitatively.

4.1 All-dielectric Resonant Metasurfaces

In this part, the results from the study of the resonances in all-dielectric metasurfaces are shown, with particular emphasis on core-shell structures. Starting with the simulation of Mie resonances in single meta-atoms, the discussion will then focus on the metasurfaces' resonant response and its dependence on the geometrical and material composition parameters. A cylindrical geometry was chosen for all meta-atom designs, both to enable a clean parametric comparison and because pillars represent one of the most fabrication-friendly and extensively studied geometries in the literature.

4.1.1 Meta-atoms Scattering

Firstly, the scattering response of single-material meta-atoms was studied.

A sweep of the pillar's radius was performed from 60 nm to 120 nm. The height of the pillars was set to 300 nm. The refractive index and the extinction coefficient values for TiO_2 and HfO_2, available in the material library of COMSOL, were taken from [54] and [55] respectively. To obtain the multipole scattering cross sections and their individual contribution to the total scattering cross section, the multipole decomposition described in section 3.1 was performed after exporting the data of the electric field and refractive index distribution inside the pillars. The results after the multipole decomposition for the TiO_2 meta-atoms are shown in Fig.16, where four different radii illustrate how the scattering is affected by the size of the pillars. As the structure gets larger in diameter, the total scattering cross section increases and gets broader. Moreover, the multipole decomposition reveals that this broadening effect is mainly caused by the decoupling between the electric and magnetic dipole, and that the lowest order Mie resonance is indeed the magnetic dipole, which appears at a longer wavelength compared to other resonances, in accordance with the theory.

The pillar cross sections shown in Fig.17 for the case of the meta-atom pillar with diameter $D = 216$ nm, illustrate how the electric and magnetic field distributions appear at $\lambda = 577$ nm when both the electric and magnetic field are excited at the same time. The strong electric field circulation inside the pillar in the zx plane corresponds to the excitation of the magnetic dipole mode, a resonance that is also visible in the magnetic field distribution in the xy plane. Moreover, a magnetic field circulation is also visible in the yz view. This circulation would cause a displacement current in the x direction within the pillar, giving rise to the electric dipole resonance which, while still being weaker than the magnetic dipole, contributes meaningfully to the total scattering cross section. At $\lambda = 425$ nm instead, the main contribution to the scattering cross section comes from the electric quadrupole, which gives rise to more complex field distributions inside the pillar as shown in Fig.18.

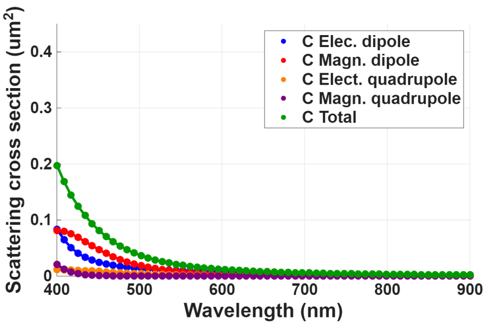

(a) Meta-atom diameter = 120 nm.

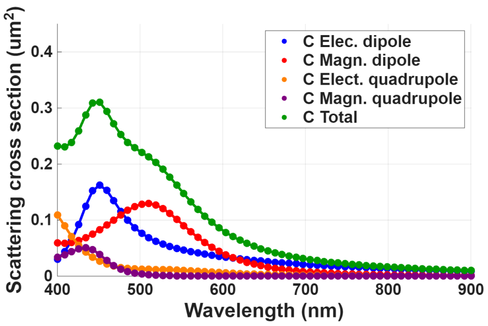

(b) Meta-atom diameter = 168 nm.

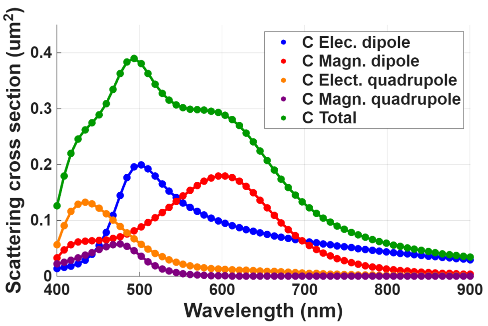

(c) Meta-atom diameter = 216 nm.

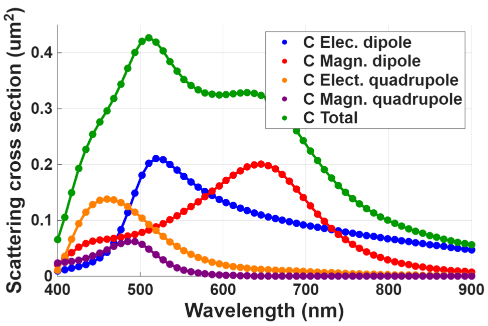

(d) Meta-atom diameter = 240 nm.

Figure 16: Scattering cross sections and their multipole components for four TiO_2 pillar meta-atoms with a fixed height of $H = 300$ nm and a varying diameter.

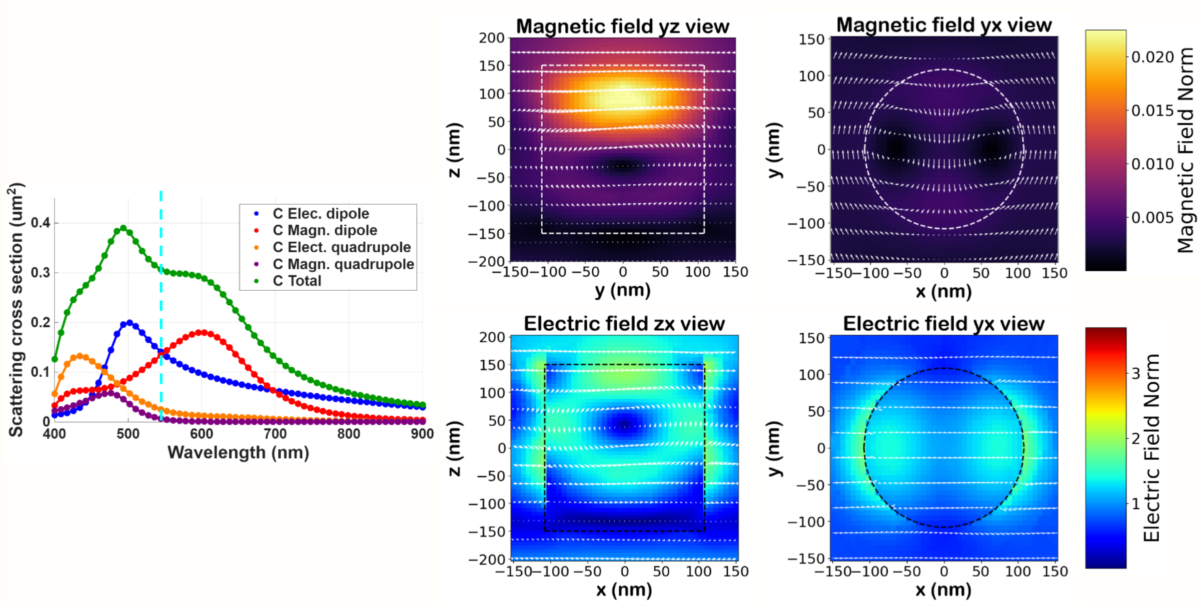

Figure 17: Cross-sections of electric and magnetic field distributions inside the TiO_2 meta-atom pillar with $D = 216$ nm for $\lambda = 577$ nm (cyan vertical line in the scattering cross section plot). The distributions in the xy plane are shown at $z = 0$ nm, while the yz and zx planes are shown at $x = 0$ nm and $y = 0$ nm respectively. The electric field circulation in the zx plane gives rise to the magnetic dipole resonance, while the magnetic field circulation in the yx plane generates a magnetic dipole resonance.

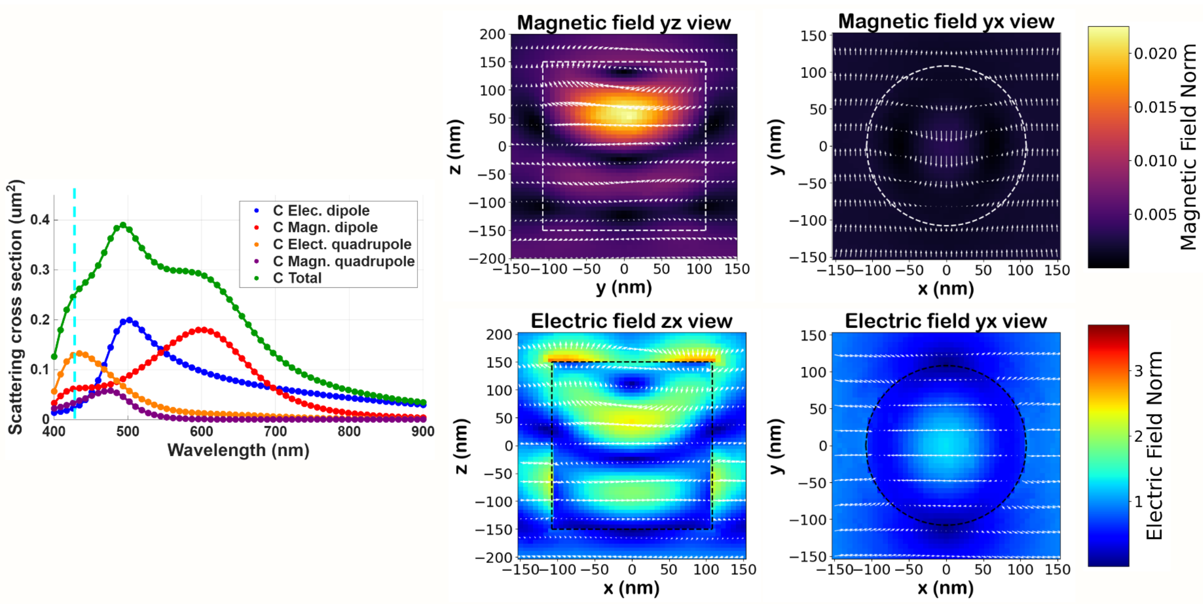

Figure 18: Cross-sections of electric and magnetic field distributions inside the TiO_2 meta-atom pillar with $D = 216$ nm for $\lambda = 425$ nm (cyan vertical line in the scattering cross section plot). The distributions in the xy plane are shown at $z = 0$ nm, while the yz and zx planes are shown at $x = 0$ nm and $y = 0$ nm respectively. The field distributions, plotted at the excitation wavelength of the electric quadrupole, are more complex compared to the ones for the electric and magnetic dipoles.

Changing the meta-atom material to HfO_2 while keeping the same simulation parameter study, shows that the scattering cross section peak shifted towards shorter wavelength compared to the previous case. The multipole decomposition reveals that this shift is caused by the appearence of the resonances at shorter wavelengths, and that their increased width has reduced and broadened the overall scattering cross section. This effect is due to the lower refractive index of HfO_2 compared to TiO_2, which confirms the relationship between the geometry and the resonances expressed in eq.1.

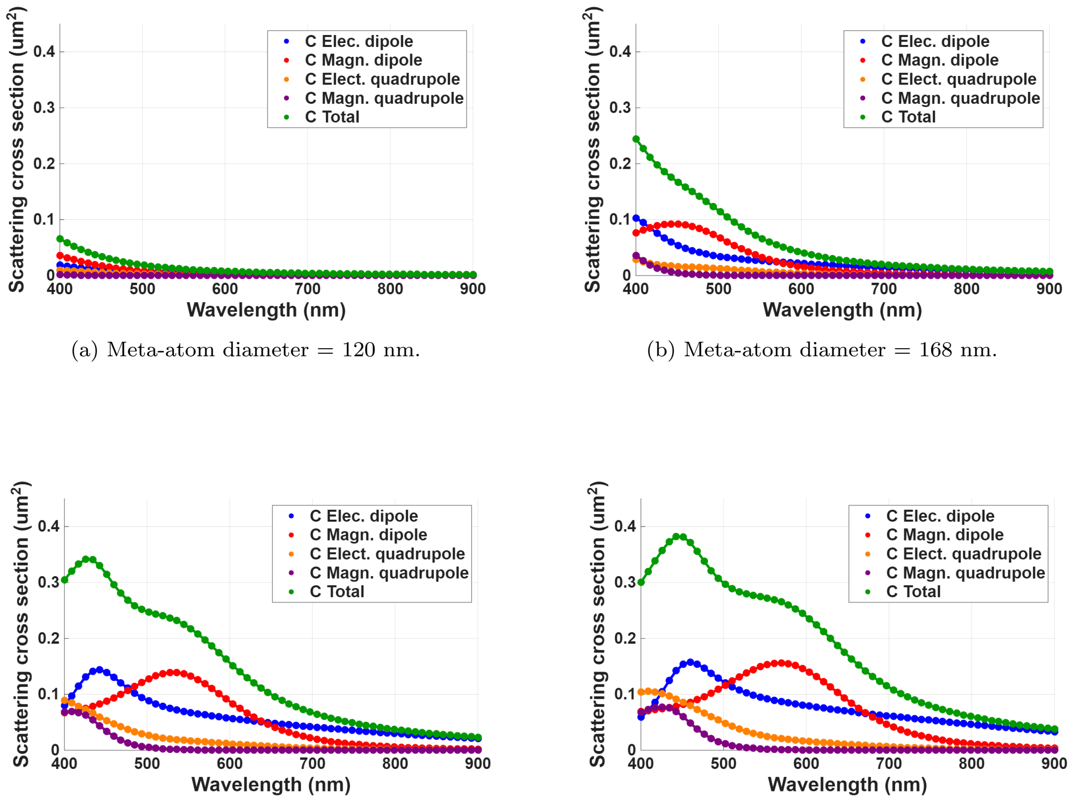

(a) Meta-atom diameter = 120 nm.

(b) Meta-atom diameter = 168 nm.

(c) Meta-atom diameter = 216 nm.

(d) Meta-atom diameter = 240 nm.

Figure 19: Scattering cross sections and their multipole components for four HfO_2 pillar meta-atoms with a fixed height of $H = 300$ nm and a varying diameter.

These two preliminary studies show that the resonant response of the meta-atoms can be efficiently tuned by continuously varying the geometry. A similar study was performed by replacing the single-material pillar with a core-shell structured pillar composed by a TiO_2 core and a HfO_2 outer shell. In this case, the geometrical parameter, i.e. the total diameter of the pillar, was kept fixed at $D = 200$ nm, while the material composition of the pillar was varied by progressively decreasing the TiO_2 diameter and increasing the thickness of the HfO_2 shell. The results are presented in Fig.20. The four plots indicate that varying the material composition effectively modifies the average refractive index of the pillar, shifting the resonances in a manner analogous to the purely geometric tuning discussed above.

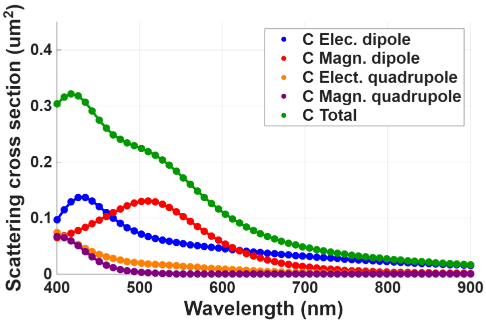

(a) TiO_2 Core diameter = 40 nm.

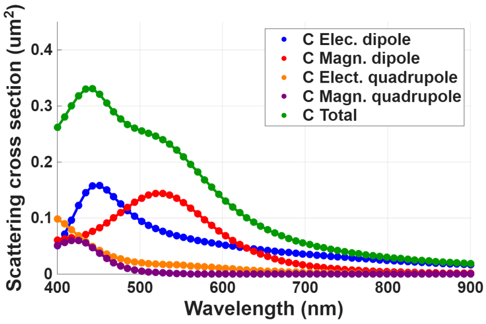

(b) TiO_2 Core diameter = 104 nm.

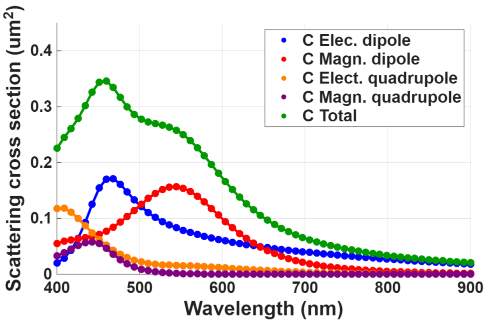

(c) TiO_2 Core diameter = 147 nm.

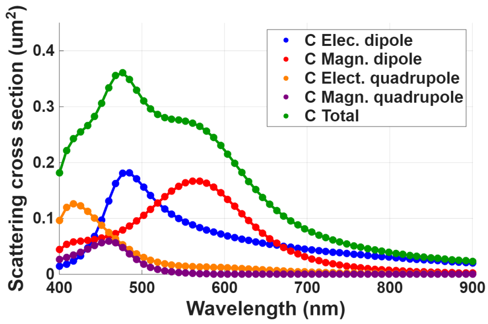

(d) TiO_2 Core diameter = 190 nm.

Figure 20: Scattering cross sections and multipole decompositions for four core-shell meta-atoms with a fixed diameter of $D = 200$ nm and height $H = 300$, each consisting of a TiO_2 core and a HfO_2 shell of varying thicknesses.

4.1.2 Geometrical Parameters Study

Moving from single pillars to metasurfaces, the first study consisted of simulating metasurfaces composed by core-shell meta-atoms with a fixed diameter $D = 200$ nm, height $H = 300$ nm and period $P = 500$ nm. The shell layer was swept from 5 nm to 80 nm thickness, which corresponds to a core diameter ranging from 190 nm to 40 nm, similarly to the single meta-atom simulation described above. For this study, both material configurations were simulated, and to determine whether the core-shell geometry could introduce new resonant features when arranged in a metasurface, or whether it simply behaves as an effective medium. Supporting simulations were carried out using single pillars made of effective materials, which were modelled as a weighted average based on the TiO2 and HfO_2 content, having a refractive index value defined as:

$$n_{eff} = \frac{n_{\mathrm{TiO_2}} V_{\mathrm{TiO_2}} + n_{\mathrm{HfO_2}} V_{\mathrm{HfO_2}}}{V_{\mathrm{TiO_2}} + V_{\mathrm{HfO_2}}} \tag{21}$$

The resulting Cauchy parameters obtained through the fitting of the effective refractive index were then used to define the effective material in COMSOL. By changing the shell layer thickness while keeping the diameter of the whole structure fixed at $D = 200$ nm, the effective material could span continuously between the refractive index values of HfO_2 and TiO_2. For example,

Fig.21 illustrates how the refractive index of the effective material varies when trying to emulate a core-shell structure with a TiO_2 core.

The transmittance heatmaps for the HfO_2 core and TiO_2 core structures shown in Fig.22 and Fig.23, respectively, reveal two distinct resonant features associated with a high degree of reflectance. In the HfO_2 core case, the resonances began to diverge when the TiO_2 shell thickness reached approximately 15 nm. The increasing TiO_2 content in the structure reduced the bandwidth of the resonances, causing their decoupling, a feature that was also noticeable in the scattering cross section study shown in Fig.20. The opposite behaviour was observed for the TiO_2 core case, where the resonances instead began to couple at a shell thickness of around 25 nm. The core-shell structure did not show any major difference from the effective material, except for an increased separation between the two resonances which was more pronounced for a shell thickness of around 40 nm.

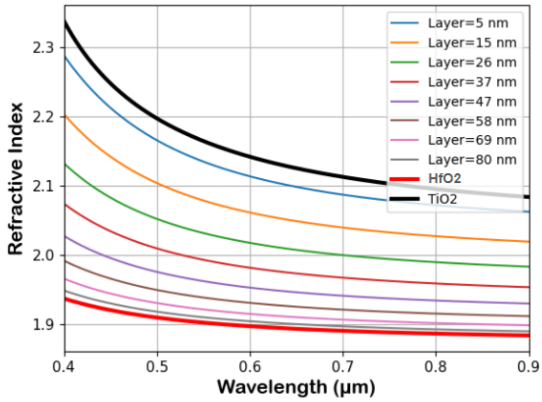

Figure 21: Effective refractive index model for a core-shell structured meta-atom having a diameter $D = 200$ nm, height $H = 300$ nm and a HfO_2 shell layer thickness ranging from 5 nm to 80 nm.

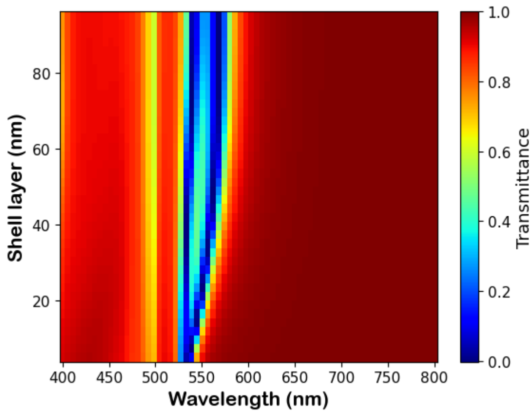

(a) Metasurface composed of core-shell meta-atoms

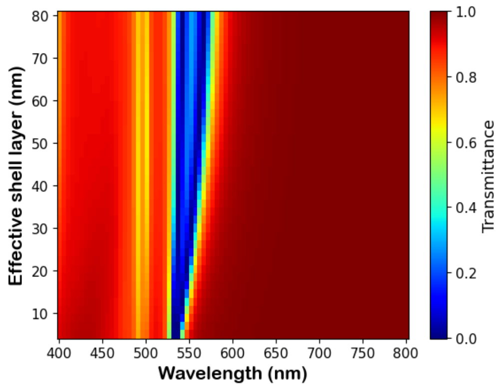

(b) Metasurface composed of effective material meta-atoms

Figure 22: Transmittance heatmaps for a) metasurface composed of meta-atoms with HfO_2 core and a TiO_2 shell layer thickness ranging from 5 nm to 80 nm and b) metasurface composed of meta-atoms with an effective material. The meta-atoms have a fixed diameter $D = 200$ nm, height $H = 300$ nm and periodicity of $P = 500$ nm.

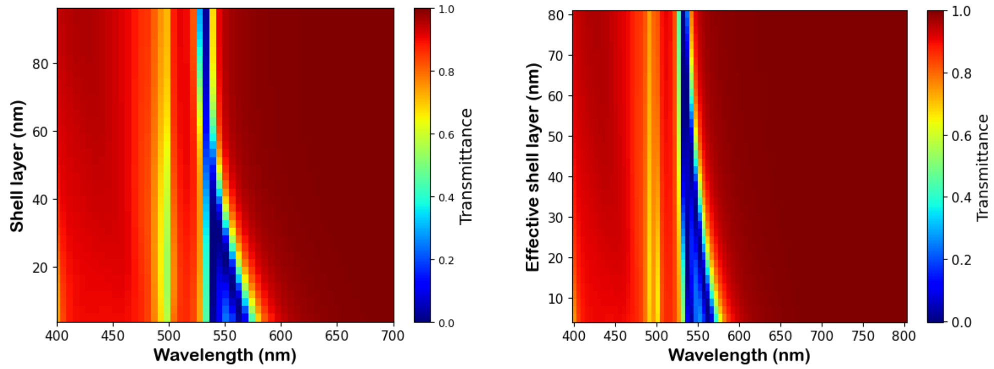

(a) Metsurface composed of core-shell meta-atoms

(b) Metasurface composed of effective material meta-atoms

Figure 23: Transmittance heatmaps for a) metasurface composed of meta-atoms with TiO_2 core and a HfO_2 shell layer thickness ranging from 5 nm to 80 nm and b) metasurface composed of meta-atoms with an effective material. The meta-atoms have a fixed diameter $D = 200$ nm, height $H = 300$ nm and periodicity of $P = 500$ nm.

A simulation study was performed to observe the effect of an increased pillar height on the resonant response of core-shell metasurfaces. The effective medium simulation approach was also carried out to compare the results and to look for possible emerging new resonant features. The periodicity of the metasurfaces was set to $P = 400$ nm, with a fixed meta-atom diameter of $D = 300$ nm. To ensure an approximate 50% composition for each dielectric material, the HfO_2 shell layer thickness was set to $T = 46$ nm, with a consequently TiO_2 core diameter of $D = 208$ nm. The transmittance heatmaps are shown in Fig.24, in which the height of the pillars was swept from 300 nm to 800 nm.

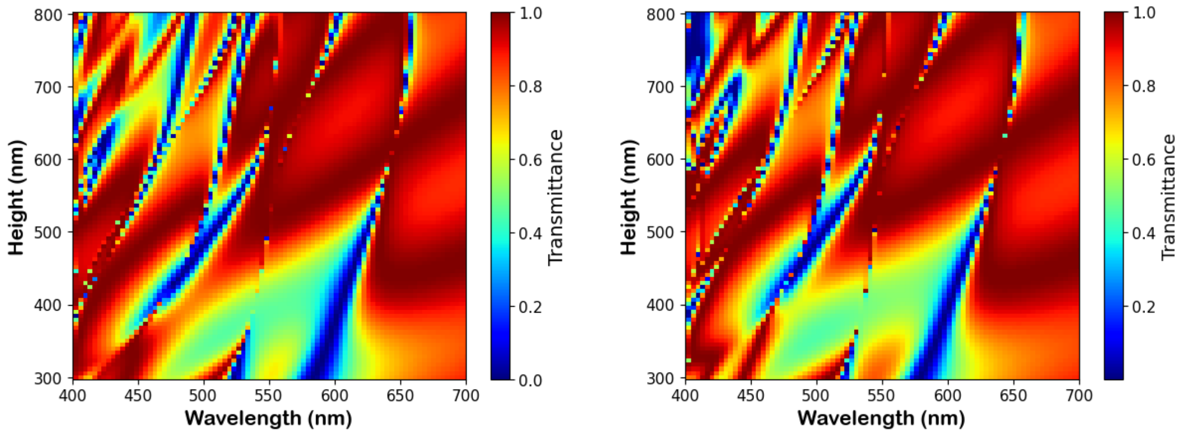

(a) Metsurface composed of core-shell meta-atoms

(b) Metasurface composed of effective material meta-atoms

Figure 24: Transmittance heatmaps for a) metasurface composed of a TiO_2 core and a HfO_2 shell layer thickness of 46 nm and b) metasurface composed of meta-atoms with an effective material. The meta-atoms have a fixed diameter $D = 300$ nm, a periodicity $P = 400$ nm and variable height ranging from 300 nm to 800 nm.

Fig. 24 reveals richer resonant features, especially for structures taller than 500 nm. The most striking of these is a resonance near 650 nm wavelength that vanishes at a pillar height of approximately 600 nm, a behaviour that may be indicative of an accidental quasi-BIC resonance, which for shorter pillars, appears as a broadband feature, progressively narrowing as the height increases, before vanishing entirely and re-emerging as a sharp resonance for slightly different geometries. As in the previous study, no new noticeable resonant effect appeared as a consequence of the layered structure of the core-shell meta-atoms, which still behave as if they were made of a single effective material.

To expand the meta-atoms geometrical parameter study, further simulations were carried out by varying the total diameter of TiO_2-core pillars between 80 nm and 200 nm. The pillar height was fixed at $H = 300$ nm, along with the periodicity $P = 500$ nm and the HfO_2 shell layer thickness $T = 26$ nm. The effective refractive index model, which has been shown to provide a good approximation for the core-shell meta-atom geometry, is plotted in Fig.25 for different radius values. At smaller diameters, the refractive index, and as a consequence, the optical response of the structure, approaches that of a purely HfO_2 metasurface, while as the diameter increases, the fixed shell thickness results in a progressively larger TiO_2 content, raising the effective refractive index accordingly.

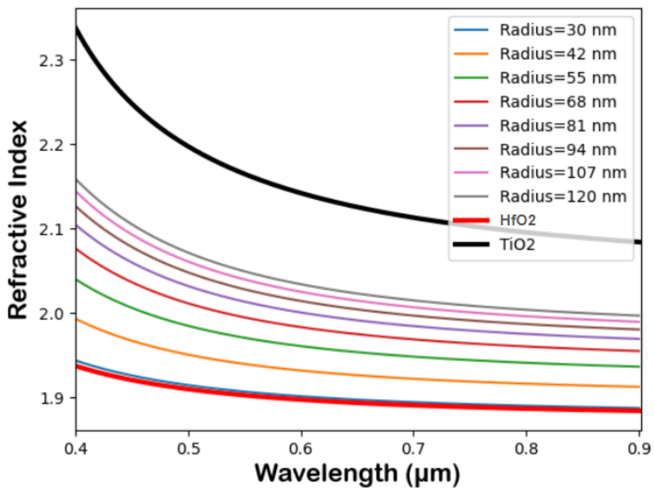

Figure 25: Effective refractive index model for a core-shell structured meta-atom having a height $H = 300$ nm, a fixed HfO_2 shell layer thickness $T = 26$ nm, and a variable radius ranging from 30 nm to 120 nm.

The simulation results are shown in Fig.26, in which the transmittance and phase heatmaps have been plotted. The transmittance plot shows two distinct resonances for structures with a diameter $D = 130$ nm or larger. As the meta-atoms grow in diameter, these two resonances begin to couple until, at around 530 nm, they interact for diameters between 177 nm and 181 nm, followed by a second decoupling and broadening for larger pillars. The interaction parameter region is associated with close to unit transmittance as shown in Fig.26a. On the other hand, the phase shift heatmap shown in Fig.26b illustrates how the transmitted light phase changed due to propagation inside the metasurface. The graph was obtained by subtracting the phase accumulation caused by an equivalent air column from the phase values extracted from the COMSOL simulation. The heatmap illustrates how, away from the resonances, the phase contribution due to the metasurface is negligible, while near the resonances, rapid phase variations occur within a narrow spectral bandwidth, driven by the strong field confinement and enhancement within the pillar. The 2π phase coverage and the close-to-unit transmittance appearing exactly at the same spectral location where the two resonances overlap and interact is an indication of the Kerker effect discussed in section 2.2. Interestingly enough, the same feature is also present in the case of full TiO_2 meta-atoms as shown in Fig.27, where with identical geometrical parameters, the Kerker effect appeared at a spectrally shifted location relative to the core-shell metasurface. In general, the refractive index of the material in use greatly affects the spectral position of the Kerker effect, and can even give rise to entirely new resonant features as illustrated in Fig.27b and Fig.27c, where two alternative refractive index datasets [56, 57] were used in combination with the one adopted throughout this thesis. The refractive index values for all three TiO_2 datasets are plotted in Fig. 28.

The final investigated parameter was the periodicity of the meta-atom pillars composing the metasurface. While not being a proper geometrical parameter, the periodicity influences the resonant response of the metasurface and represents an additional degree of freedom for spectral tuning of the resonances, without requiring any modification to the meta-atoms geometry. Four simulations were carried out, two with single-material meta-atoms, and two with core-shell pillars exploring both material combinations, one having a TiO_2 core and HfO_2 shell, and one with the opposite material configuration. The diameter was fixed at $D = 300$ nm, height $H = 300$ nm and for the core-shell metasurfaces, the shell layer thickness was kept fixed at $T = 46$ nm. The periodicity was swept from 200 nm to 500 nm. All four plots show four different resonant features, with the exception of Fig.29c, in which only three of those are visible. The two most noticeable are the high reflectance resonances caused by the excitation of the electric and magnetic dipoles between 400 nm and 550 nm, which appear up across all the studied periodicities except for the HfO_2 metasurface, in which no resonances are observed for a periodicity of 260 nm or under. These two resonances are spectrally distinct for the case of HfO_2-based metasurfaces, while they overlap for the TiO_2-based ones. A third resonance is visible for periodicities between 350 nm and 450 nm approximately, within a spectral window of 400 nm and 450 nm. Its absence in Fig.29c indicates that this feature originates from the higher refractive index of TiO_2, pointing to a possible higher-order Mie resonance. The fourth and final resonance, indicated by the dashed black lines, appears when $P = \lambda$ for all four simulations. In fact, it originates from the Rayleigh anomaly discussed in section 2.2.1, in which the evanescent diffraction orders can still propagate along the surface of the metasurface, leading to a dip in the transmittance caused by the lattice resonance and its non-locality.

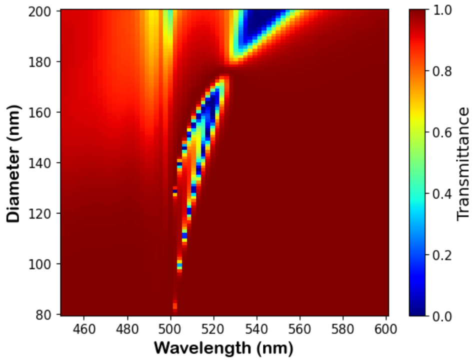

(a) Transmittance heatmap for a core-shell metasurface with variable diameter meta-atoms.

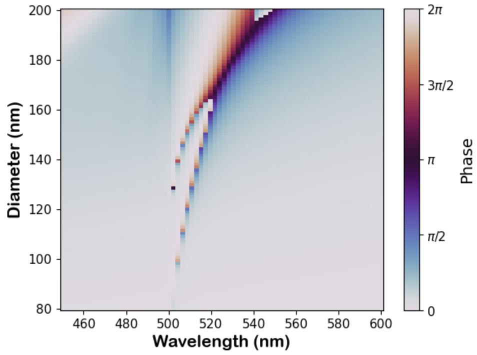

(b) Phase heatmap for a core-shell metasurface with variable diameter meta-atoms.

Figure 26: a) Transmittance and b) phase heatmaps for a metasurface composed of a TiO_2 core and a HfO_2 shell layer thickness of 26 nm. The meta-atoms have a fixed height $H = 300$ nm, a periodicity $P = 500$ nm and variable diameter ranging from 80 nm to 200 nm.

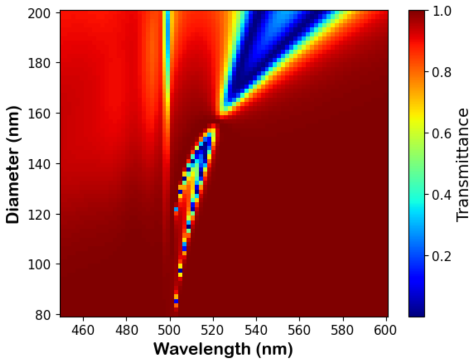

(a) Transmittance heatmap for a TiO_2 metasurface with variable diameter meta-atoms. Refractive index data taken from [54]

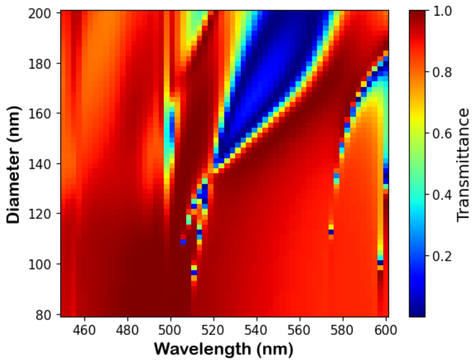

(b) Transmittance heatmap for a TiO_2 metasurface with variable diameter meta-atoms. Refractive index data taken from [56]

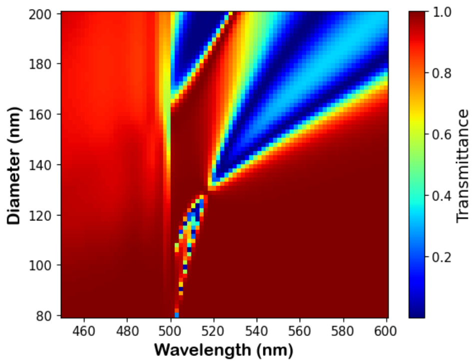

(c) Transmittance heatmap for a TiO_2 metasurface with variable diameter meta-atoms. Refractive index data taken from [57]

Figure 27: Transmittance heatmaps for TiO_2 metasurfaces with variable diameter meta-atoms. Each simulation was run with a different TiO_2 refractive index library available in COMSOL.

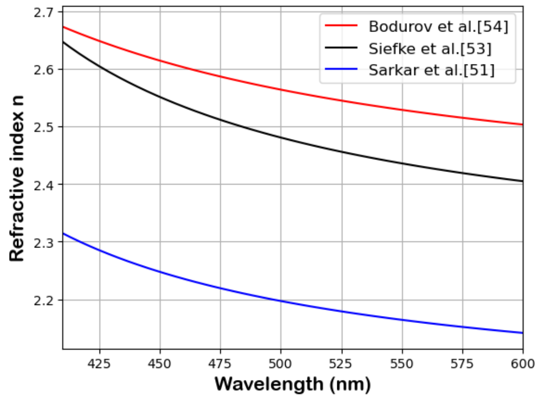

Figure 28: Refractive index values of TiO_2 taken from three different datasets available in COMSOL.

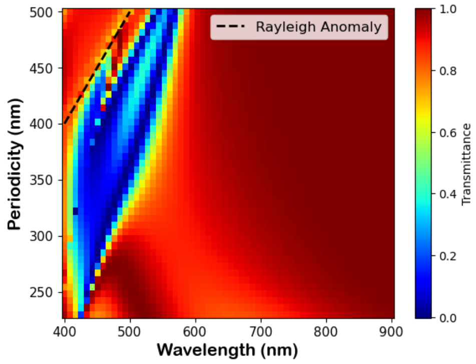

(a) Transmittance heatmap for a TiO_2 metasurface with a variable periodicity.

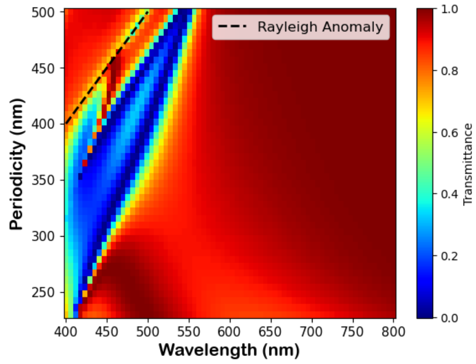

(b) Transmittance heatmap for a core-shell metasurface with a TiO_2 core and a variable periodicity.

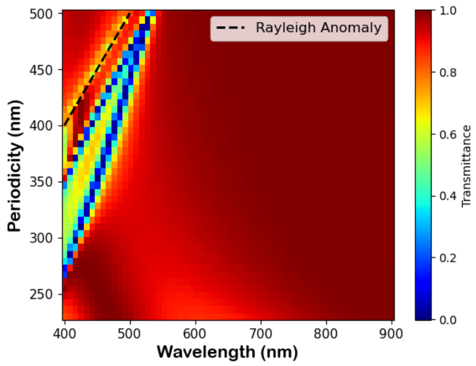

(c) Transmittance heatmap for a HfO_2 metasurface with a variable periodicity.

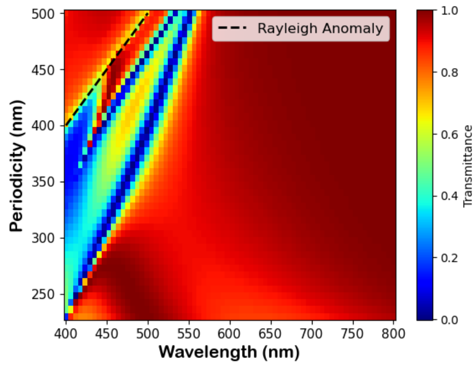

(d) Transmittance heatmap for a core-shell metasurface with an HfO_2 core and variable periodicity.

Figure 29: Transmittance heatmaps for a) metasurface composed of TiO_2 meta-atoms b) metasurface composed of meta-atoms with TiO_2 core and a HfO_2 shell layer thickness of 46 nm c) metasurface composed of HfO_2 meta-atoms d) metasurface composed of meta-atoms with HfO_2 core and a TiO_2 shell layer thickness of 46 nm. The meta-atoms have a fixed diameter $D = 300$ nm, height $H = 300$ nm and variable periodicity of P ranging from 200 nm to 500 nm. The Rayleigh anomaly is indicated by the black dashed line appearing in all four plots. The electric and magentic dipole resonances are present in all the plots, while the higher-order resonant feature visible in a), b) and d) is not present in the HfO_2 metasurface study shown in c).

4.2 Metasurfaces for Nonlinear Optics

As described in section 2.3, the field enhancements and relaxed phase matching conditions enabled by metasurfaces make them an interesting technology to be studied in the field of nonlinear optics. This part will show the results of a metasurface concept for harmonic generation. The metasurface has been designed to be placed inside a multipass cell, an optical device in which a laser pulse propagates through a nonlinear or dispersive medium multiple times via successive reflections off mirrors. The goal for this concept is the realisation of a setup to boost harmonic generation efficiencies using resonant metasurfaces. The metasurface was designed to work at a wavelength of $\lambda_0 = 1030$ nm and optimised for third harmonic generation at $\lambda_3 = 343$ nm, due to the impossibility of generating the second harmonic with amorphous materials. The light source for this concept is a pulsed laser with a 180 fs pulse duration and a bandwidth of 10 nm centered at λ_0. While materials with higher $\chi^{(3)}$ exist, the studied materials were TiO_2 and HfO_2, this choice was made due to their ease of fabrication, wide transparency windows and fabrication expertise at Lund Nano Lab.

4.2.1 TiO_2 Resonant Metasurface

TiO_2-based metasurfaces were first studied due to its higher $\chi^{(3)}$ compared to HfO_2.

As seen previously, to find suitable resonances, the meta-atoms diameters have to approach at least a value $D \approx 500$ nm dictated by eq.1, which imposes a minimum threshold for the pillars diameters when working at 1030 nm. This can be seen in Fig.30, where diameter and height were swept for a TiO_2 based metaurface having a periodicity $P = 550$ nm.

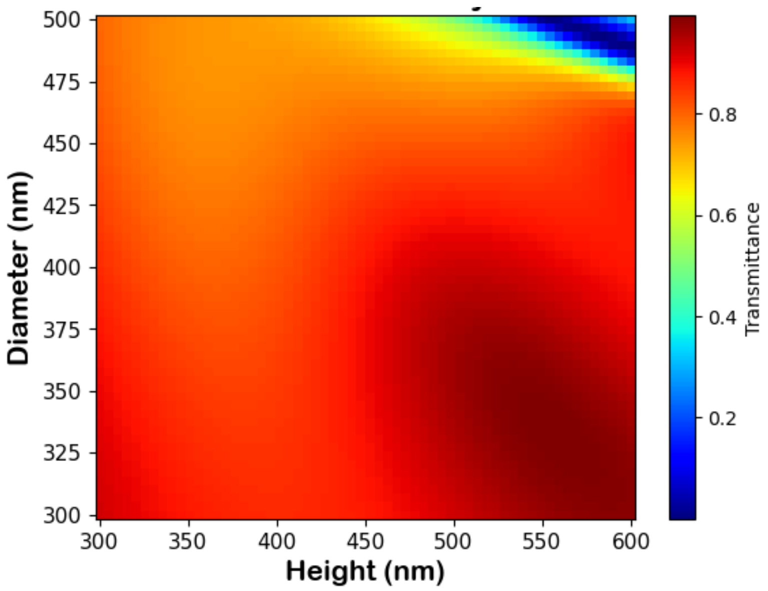

Figure 30: Transmittance heatmap for a TiO_2-based metasurface with a periodicity $P = 550$ nm at $\lambda = 1030$. The diameter D and the height H of the pillars were swept from 300 nm to 500 nm, and from 300 nm to 600 nm respectively.

A resonance indicated by an increased reflectance appeared only when the pillars reached a height between 500 nm and 600 nm and a diameter $D \approx 475$ nm at least. Because the diameter of a pillar can only be lower than the periodicity of the metasurface, the distance between pillars became longer than the third harmonic λ_3, making the metasurface design intrisically diffractive at this wavelength. This is usually not a problem in setups where the light passes trhough the metasurface only one time, but it could potentially be an issue for multi-passes, due to a consequently lower total third harmonic generation efficiency.

Nevertheless, a second simulation was then run by fixing the height at $H = 550$ nm while sweeping the diameter from 460 nm to 620 nm and the periodicity from 650 nm to 700 nm. The results are shown in Fig.31. The simulation shows a resonance for pillar diameters ranging from 520 nm to 540 nm with little dependence on the periodicity of the metasurface, probably caused by a localized resonant response within the pillars and signaling a high degree of locality in the metasurface design. This resonance divides the parameter space into two regions: a high-transmittance regime for diameters above 540 nm, and a lower transmittance regime where values do not exceed approximately 0.5.

A third simulation was then performed to study the response at the third harmonic $\lambda_3 = 343$ nm, with the geometrical parameters being $H = 550$ nm, $P = 670$ nm. The diameter was swept from 530 nm to 550 nm, where the resonance appeared at this specific periodicity. As shown in Fig.32 though, the metasurface experiences absorption well over 80% due to the TiO_2 content. In fact, at $\lambda_3 = 343$ nm , TiO_2 is still partially absorbing, as λ_3 falls at the bandgap edge of TiO_2. For this reason, the metasurface design based on TiO_2 was discarded.

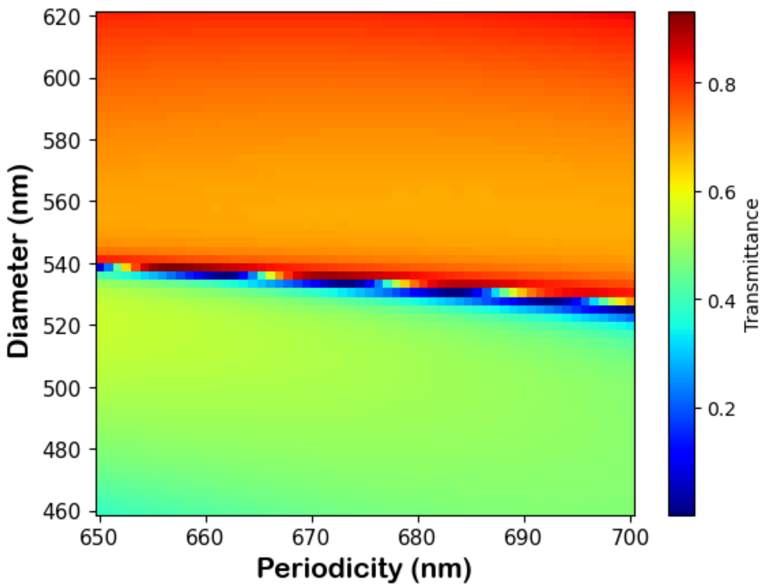

Figure 31: Transmittance heatmap for a TiO_2-based metasurface composed by pillars with a fixed height $H = 550$ nm at $\lambda = 1030$. The diameter D and the periodicity P of the pillars were swept from 460 nm to 620 nm, and from 650 nm to 700 nm respectively.

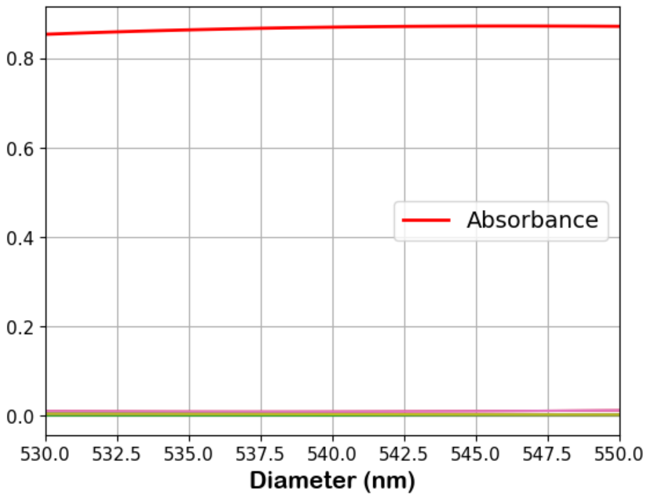

Figure 32: Absorbance (red line) and transmission orders (colored lines) for a TiO_2-based metasurface at $\lambda = 343$ nm. The pillar's height and periodicity were fixed at $H = 550$ nm and $P = 670$ nm respectively, while the diamater was swept from 530 nm to 550 nm.

4.2.2 HfO_2 Resonant Metasurface

HfO_2-based metasurfaces were subsequently investigated due to the material's wider transparency window. The same simulation parameters choice for obtaining Fig-31 were used, with the only difference being the meta-atoms' material. Unlike the TiO_2 case, the resonance appeared to be period-dependent, shifting towards smaller diameters as the periodicity increased, indicating a higher degree of non-locality of the resonance caused by a weaker field confinement due to the lower refractive index of HfO_2.

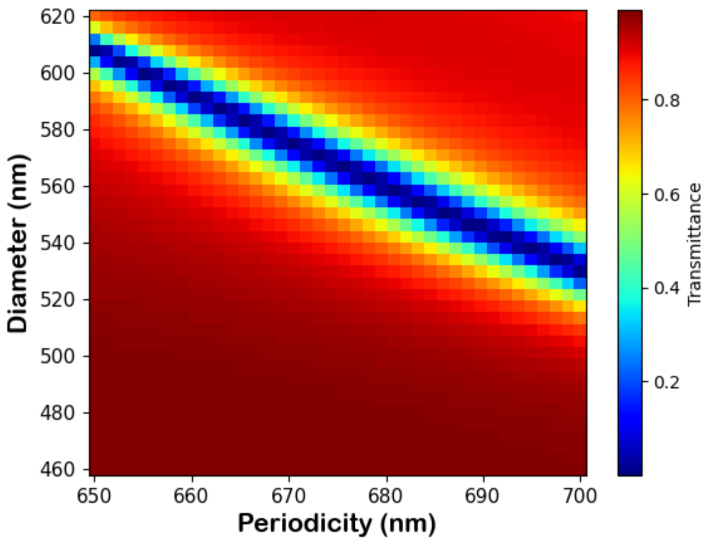

Figure 33: Transmittance heatmap for a HfO_2-based metasurface composed by pillars with a fixed height $H = 550$ nm at $\lambda = 1030$. The diameter D and the periodicity P of the pillars were swept from 460 nm to 620 nm, and from 650 nm to 700 nm respectively.

Up to this point, the placement of the metasurface inside the MPC had not yet been determined, but looking at Fig.33 as well as the previous plots, the resonances mostly appeared as dips in the transmission spectrum, with strong field enhancements correlated with high reflectance. Designing the metasurface to operate in transmission would allow for simultaneously high transmittance and high field enhancements only at the Kerker effect, a feature that was not visible at the investigated geometrical parameters and wavelength. This motivated a re-design of the structure to include a 300 nm Ag layer at the bottom of the structure, with a 1 μm layer sitting between the pillars and the metal. Working in reflection, the metasurface is then designed to be placed directly on one or both mirrors, with the simulation shown in Fig.34 confirming the near-unit reflectance at λ_0 and for the source bandwidth. The origin of

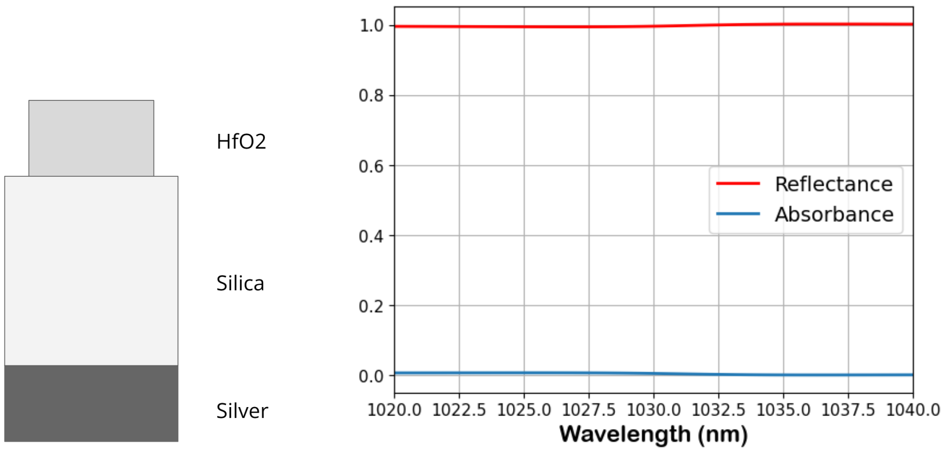

(a) (b)

Figure 34: a) Design illustration of the HfO_2-based metasurface structure to work in reflection b) Reflectance and absorbance spectrum centered at $\lambda = 1030$ for a HfO_2-based metasurface. The pillar's height, periodicity and diameter were fixed at $H = 550$ nm, $P = 670$ nm and $D = 586$ nm respectively.

the resonance seen in Fig.33 was clarified by plotting the field distributions inside a meta-atom with $D = 586$ nm, and a metasurface periodicity of $P = 670$ nm shown in Fig.35 and 36. A magnetic dipole mode is clearly excited for wavelengths shorter than λ_0 within the bandwidth, while two opposite electric dipoles can be seen for wavelengths higher than λ_0, indicating a possible electric quadrupole resonance inside the pillar. The resonance shown in Fig.33 can then be related to this two slightly decoupled resonances, which could potentially achieve a high field enhancement within the working bandwidth. In fact, the electric field distributions show a ten-fold increase in the field magnitudes inside the pillars in the near vicinity of the fundamental wavelength.

Successively, a simulation for wavelengths ranging from $\lambda = 341$ nm to $\lambda = 345$ nm with the same geometrical parameters was run to observe the behaviour of the metasurface at the third harmonic. The results plotted in Fig.37 show that, even when becoming diffractive, the metasurface could still reflect around 45% of the incoming light at λ_3 along the reflectance 0^{th} order. Nonetheless, the inclusion of Ag in the structure would cause significant absorption ranging between 20% and 30 % of the incoming light at the studied wavelengths.

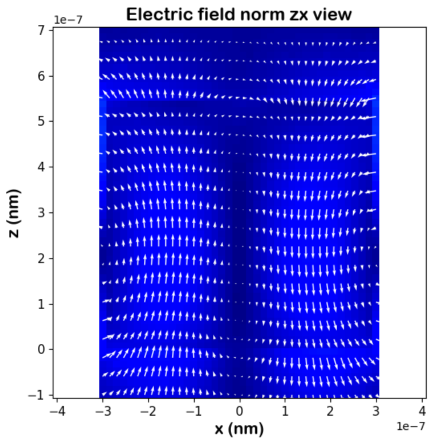

(a) $\lambda = 1028$ nm

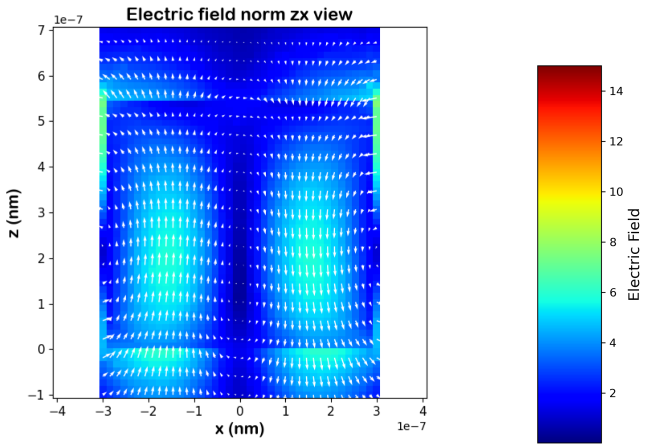

(b) $\lambda = 1028$ nm

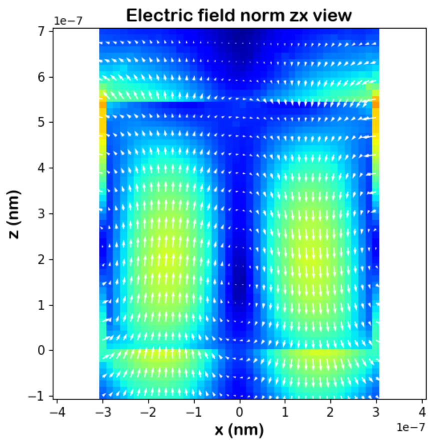

(c) $\lambda = 1030$ nm

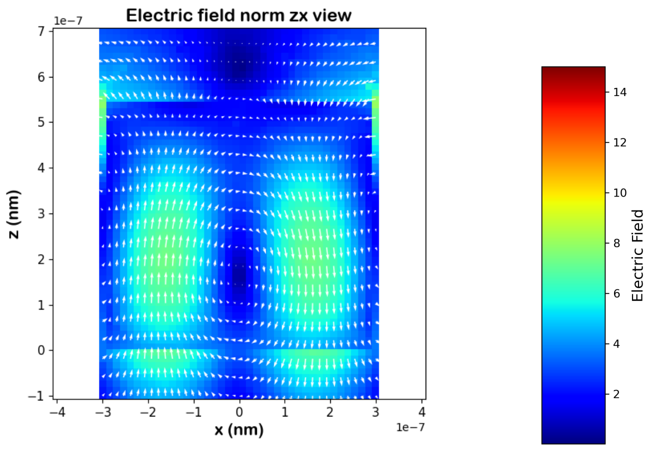

(d) $\lambda = 1034$ nm

Figure 35: Electric field norm distribution inside the reflective HfO_2 metasurface's pillar having a diameter $D = 586$nm, height $H = 550$ nm and periodicity $P = 670$ nm.

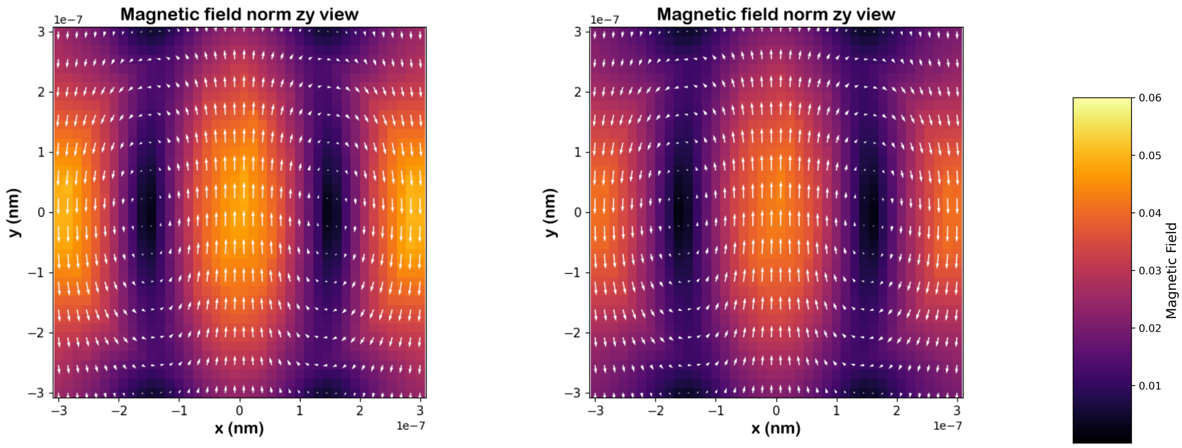

(a) $\lambda = 1026$ nm (b) $\lambda = 1028$ nm

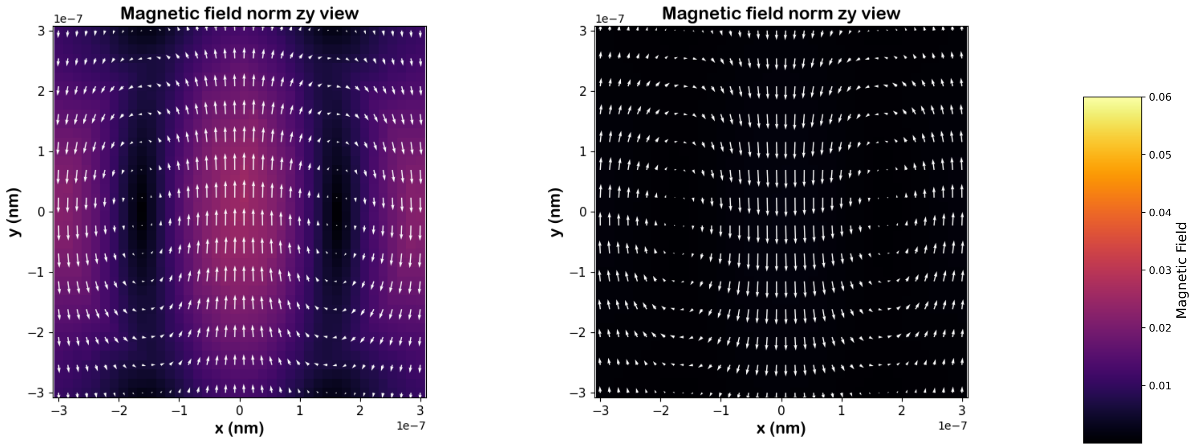

(c) $\lambda = 1030$ nm (d) $\lambda = 1034$ nm

Figure 36: Magnetic field norm distribution inside the reflective HfO_2 metasurface's pillar having a diameter $D = 586$nm, height $H = 550$ nm and periodicity $P = 670$ nm.

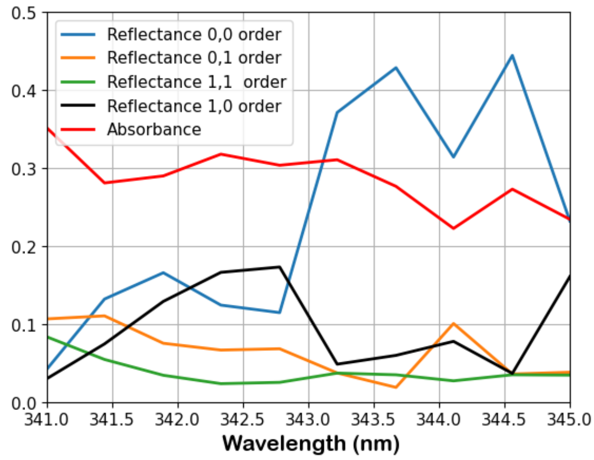

Figure 37: Absorbance and reflectance spectra centered at $\lambda = 343$ nm for the reflective HfO_2 metasurface. The diameter was fixed at $D = 586$nm, the height at $H = 550$ nm and the periodicity at $P = 670$ nm.

4.3 Fabrication

After the simulation studies, to test the predictions and observe the resonant features, a selection among the simulated designs had to be made to fabricate and characterize the response of the metasurfaces. The choice had to take into consideration both the presence of interesting features and the ease of fabrication.

Within all the simulation results, two metasurface designs having $H = 300$ nm, $P = 500$ nm and $D = 140$ nm and 145 nm respectively, were chosen from the diameter parametric study shown in Fig.27 exhibiting the Kerker effect. In particular, the designs were selected from Fig.27b because the refractive index values [56] used for the simulation were the most compatible with the ones observed for TiO_2 deposited with ALD at LNL.

From a fabrication standpoint, these designs were also the most practical choice since the other simulated geometries featured larger pillar diameters or high aspect ratios, which would have resulted in longer EBL exposures or higher risks of fabrication defects. The core-shell structured design was excluded for similar reasons, its fabrication would have required a more complex process flow and the simulations did not reveal any new resonant features or increased field confinement compared to an effective material that would justify the added effort.

Scanning electron microscopy (SEM) was used to observe the pillars on the metasurface and verify that the fabrication process had successfully replicated the designed geometries. To prevent the charge buildup on the surface due to the device being made of dielectric materials, a thin Pt/Pd layer was deposited on the metasurface to prevent static charge buildup, which would otherwise distort the electron trajectories and produce artifacts in the acquired images. It has to be noted that this SEM inspection was performed only after the optical characterization, as the metallic coating inevitably modifies the sample structure.

The SEM results presented in Fig. 38, 39 and 40 for both metasurfaces, show that the ALD run failed to fill the cavities completely, creating pillars with hollow cores having diameters of 38.8 nm for the $D = 140$ nm metasurface and 43.4 nm for the $D = 145$ nm metasurface. The missing material at the center was caused by the ALD tool running out of the TiO_2 precursor. Nonetheless, the fabrication process was successful in creating pillars with the intended geometrical parameters as demonstrated by Fig.38, showing pillars having diameters $D \approx 140$ nm and $D \approx 145$ nm, and by Fig.39, where pillar heights of $H \approx 300$ nm were obtained by directly measuring the length of a fallen pillar and by tilting the metasurface by 30° and retrieving the actual height from $H = H_{proj}/sin(30°)$, where H_{proj} is the projected height obtained from the SEM images. A periodicity $P \approx 500$ nm was also measured as seen in Fig.40.

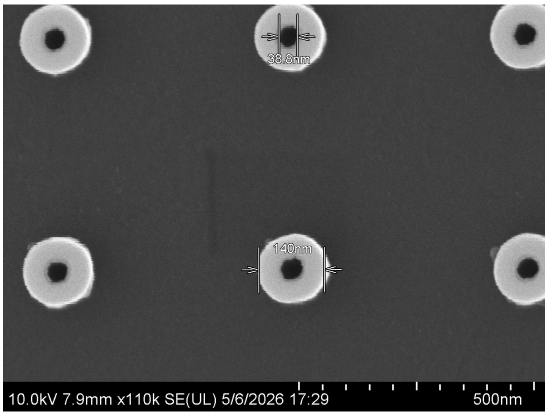

(a) SEM image of the 0.5×0.5 mm^2 metasurface, presenting a diameter $D = 140$ nm and an hollow core of diameter 38.8 nm.

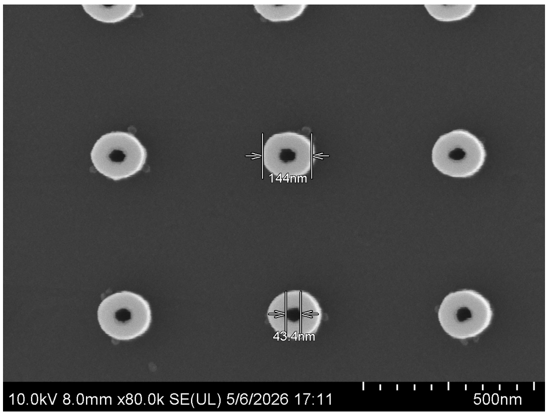

(b) SEM image of the 1×1 mm^2 metasurface, presenting a diameter $D = 145$ nm and an hollow core of diameter 43.4 nm.

Figure 38: SEM images captured at normal incidence with respect to the metasurfaces. a) SEM image of the 0.5×0.5 mm^2 metasurface with intended diameter $D = 140$ nm. b) SEM image of the 1×1 mm^2 metasurface with intended diameter $D = 145$ nm.

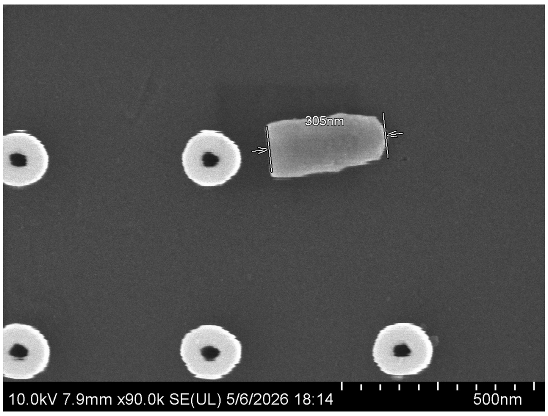

(a) SEM image captured at normal incidence where the height of a fallen pillar has been measured.

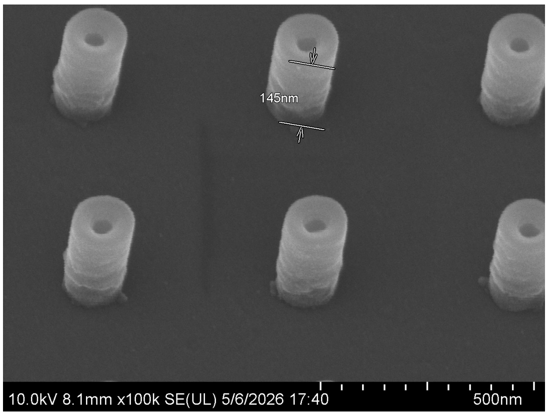

(b) SEM image captured at an inclination angle of 30° between the metasurface normal and the detector.

Figure 39: SEM images of the 0.5×0.5 mm^2 metasurface captured at a) normal incidence and b) at an angle of 30° to measure the height of the pillars. The height was measured from a fallen pillar as well as calculated by knowing the angle of inclination and the projected value of 145 nm.

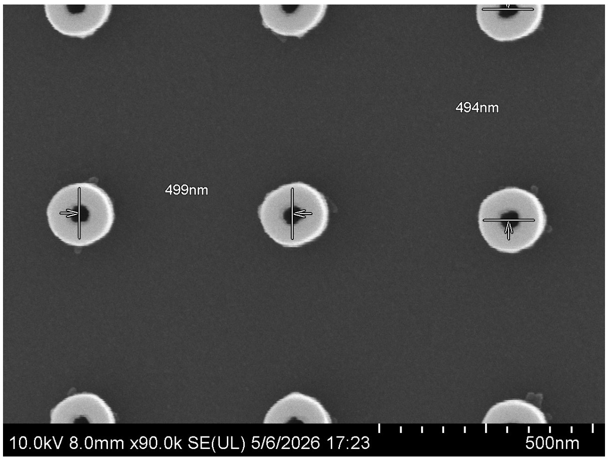

Figure 40: SEM image of the 1×1 mm^2 metasurface captured at normal incidence presenting a periodicity of $494 \sim 499$ nm.

4.4 Optical Characterization

As previously mentioned, the two designs were fabricated to experimentally observe the resonance in the vicinity of the Kerker effect, and how it transforms when the diameter of the pillars is changed. Fig.41 illustrates the location of the two metasurfaces in the parametric simulation results, as well as their expected spectrum.

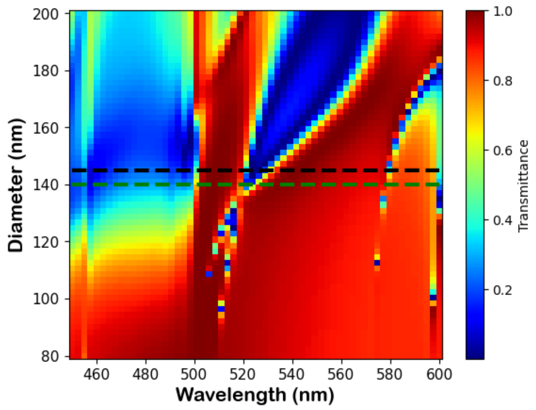

(a) 0th order transmittance heatmap.

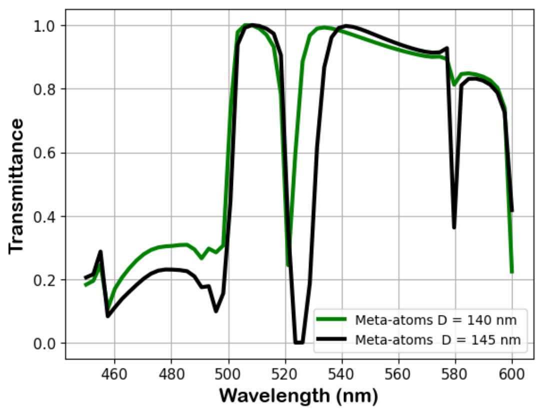

(b) 0th order transmittance line profiles.

Figure 41: a) Heatmap of the 0th order transmittance spectrum resulted from the diameter parametric study of the TiO_2 metasurface with an height $H = 300$ nm and periodicity $P = 500$ nm and b) extracted line profiles for diameters $D = 140$ nm (green line) and $D = 145$ nm (black line).

To experimentally observe the feature seen in Fig.41b, the optical characterization was performed by measuring the transmission spectra of the two fabricated metasurfaces using the white light spectroscopy setup detailed in section 3.3. The spectrometer recorded the detector counts as a function of wavelength by collecting the light from the multi-mode fiber output every 500 μs, with the displayed results on the computer being averaged over 80 acquisitions. First, to isolate the spectral response of the metasurfaces from the substrate, a reference intensity spectrum I_{ref} was acquired by letting the beam propagate only through the silica. This spectrum was then used to normalize the spectra recorded by directing the beam towards each metasurface, returning a transmittance $T = I_{MS}/I_{ref}$. This normalization removed the losses appearing only due to the substrate shown in Fig.42, and allows direct comparison with the transmittance spectra obtained from the simulations.

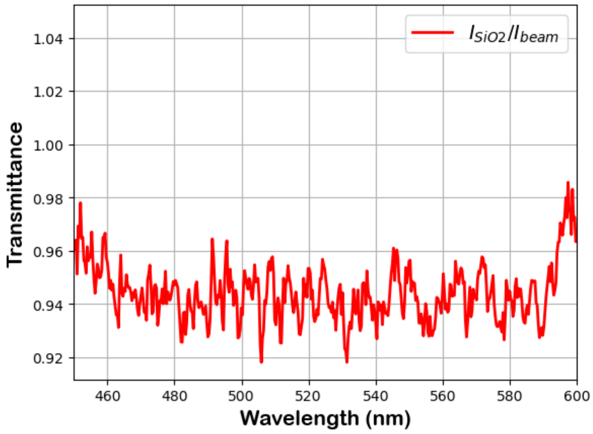

Figure 42: Transmittance spectrum of the fused silica substrate substrate calculated by dividing the detector data of the beam passing through the substrate I_{SiO2} by the data of the beam I_{beam}.

The spectra together with the transmittance simulations results are presented in Fig.43. The experimental results for both metasurfaces show a much higher transmittance compared to the simulations, this difference is especially evident at wavelengths < 500 nm, where the meta-atom periodicity Λ becomes larger than the incident wavelength and the metasurface enters the diffraction regime. Moreover, the resonance feature at 521 nm observed in the simulations is not distinguishable in the experimental results. The noise visible in the recorded spectra in Fig.43a can be attributed to modal interference within the multi-mode fiber that connects the integrating sphere to the spectrometer. In fact, during the data acquisition, the interference pattern was observed to fluctuate and momentarily vanish after touching the fiber, a result of the phase randomization between modes induced by the movement. Despite the interference noise, a slight decrease in transmittance can be seen for $\lambda > 520$ nm for the metasurface composed of meta-atoms with a diameter $D = 140$ nm compared to the one having meta-atoms with $D = 145$ nm. On the other hand, for $\lambda < 500$ nm the metasurface with $D = 140$ nm has a higher transmittance, an effect that is visible in the simulation results as well, but that could also be explained by the fact that the metasurface dimensions were comparable to the beam diameter as seen in Fig.15, letting parts of the beam partially propagate only through the glass, lowering the diffraction efficiency as a consequence.

One possible explanation for the missing resonance in the experimental results is the limited spectrometer's resolution of 20 nm, which could average out the sharp feature, causing a transmittance decrease over a much broader spectral range compared to the resonance bandwidth of around $2 \sim 5$ nm observed in the simulations. The low resolution of the spectrometer could also explain why the transition to the diffractive regime at 500 nm seems to be gradual instead of abrupt like in the simulation results. Applying a moving average with an interval of 20 nm over the simulated spectra to mimic the resolution of the spectrometer does indeed produce a more gradual shift at 500 nm and affect the visibility of the resonance as seen in Fig.44, especially for the metasurface with meta-atoms with $D = 140$ nm. For the other metasurface, the resonant feature can still be seen after the convolution, even though its bandwidth and transmittance are distorted compared to the simulation.

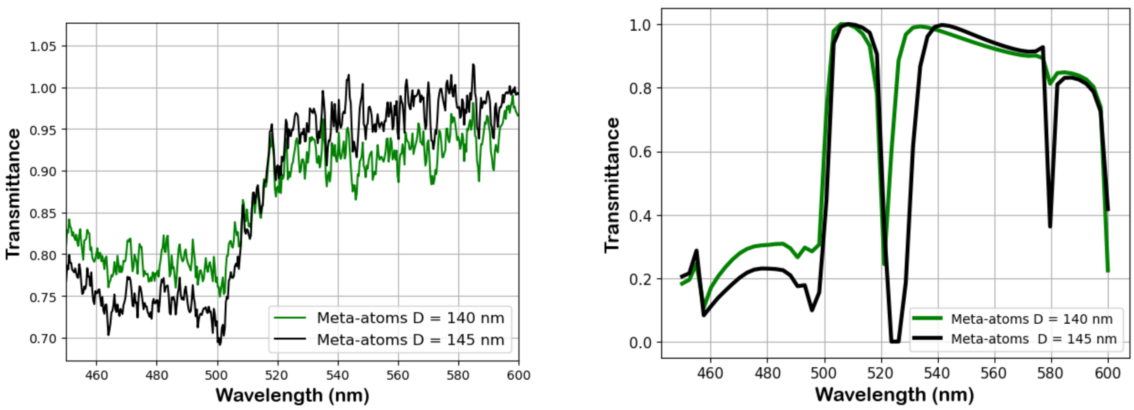

(a) Experimental normalized transmittance spectra.

(b) Simulated transmittance spectra.

Figure 43: a) Experimental and b) simulated transmittance spectra of the two metasurfaces.

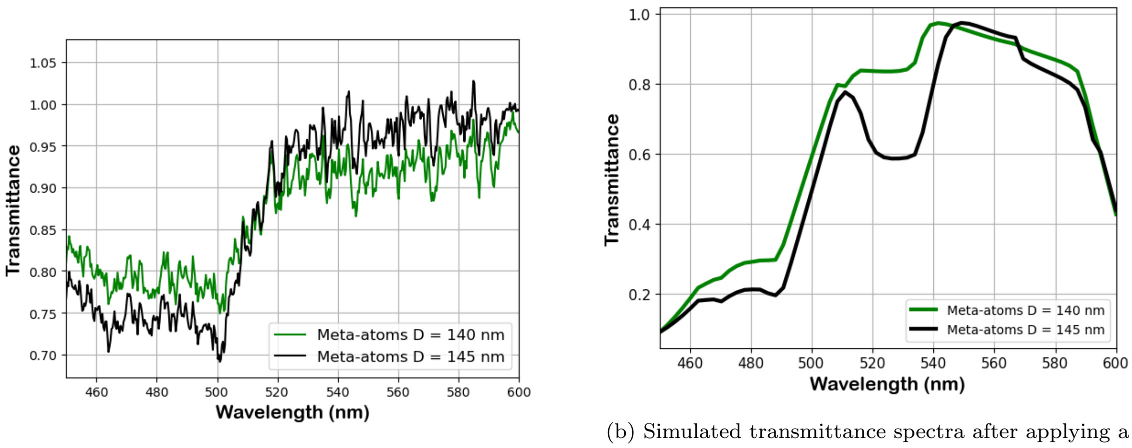

(a) Experimental normalized transmittance spectra.

(b) Simulated transmittance spectra after applying a moving average

Figure 44: a) Experimental transmittance spectra and b) simulation transmittance spectra after applying a moving average with a 20 nm window to mimic the effect of the spectrometer's resolution.

The possible contribution of the metasurface hollow core structure to the resonant response was then investigated to see if the uncomplete deposition could have explained the missing feature in the experimental results.

A simulation was run by replicating the actual pillar structure and dimensions measured through the SEM images, and the results of this study are shown Fig. 45b. The resonance at 520 nm remains visible for both metasurfaces, but the the hollow core seems to affect the diffraction efficiencies, causing an increase in transmission for $\lambda < 500$ nm, as well as the complete disappearance of the sharp resonant feature previoulsy observed at 580 nm.

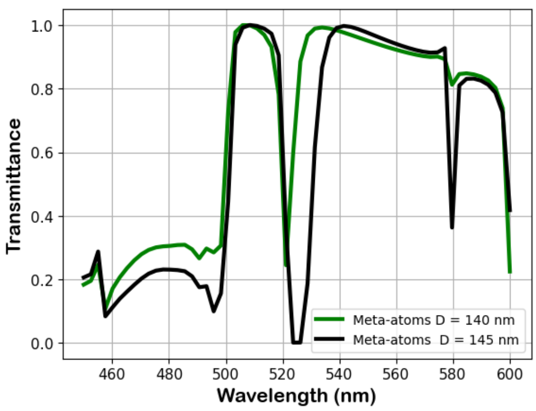

(a) Simulated transmittance spectra of the two metasurfaces having completely filled pillars.

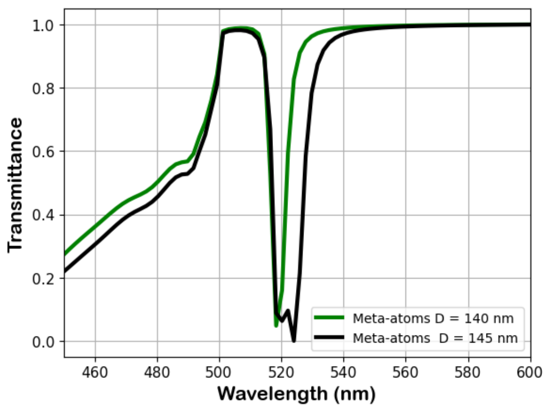

(b) Simulated transmittance spectra of the two hollow core metasurfaces.

Figure 45: Simulated transmittance spectra for the a) metasurfaces with completely filled pillars and b) metasurfaces with hollow core pillars replicating the fabrication results.

5 Conclusions and Outlook

In this thesis, the resonant response of all dielectric TiO_2 and HfO_2 metasurfaces has been studied, with particular emphasis on metasurfaces with meta-atoms having core-shell geometries. The work was structured towards two main goals, with the first one being focused on the investigation of the core-shell structured metasurfaces and how this geometry affects the resonant response, while the second one was dedicated in designing a metasurface concept optimised for third harmonic generation inside a multipass cell.

The study, performed through simulations in COMSOL, firstly showed that TiO_2 and HfO_2 cylindrical pillars could sustain multiple and overlapping resonant modes, with the magnetic dipole appearing as the lowest order mode in agreement with the theory. The multipole decomposition of the scattering cross section revealed that the electric and magnetic dipole contributions were the dominating mode compared to the higher order Mie resonances. Consistently with the theory, replacing TiO_2 with HfO_2 at the same geoemetrical parameters and spectral range caused a blueshift of the resonances due to the lower refractive index of the material. The core-shell structure scattering study, performed at a fixed total diamater with a varying shell thickness, showed that the material composition acted as an additional degree of freedom to tune the resonant response of the scatterers.

In the metasurfaces geometry study, the effects of the meta-atoms height, diameter, periodicity and shell thickness on the resonances were simulated by sweeping one geometrical parameter at a time while keeping the others fixed. Across all configurations, the simulations showed that the core-shell geometry did not lead to new resonant emerging features, but instead acted on the resonances like a tunable effective material varying between the optical properties of pure TiO_2 and HfO_2. The height sweep revealed richer resonant features for taller pillars, including a feature near 650 nm that progressively narrowed with increasing height before disappearing, consistent with the behaviour of an accidental quasi-BIC. The sweep of the period showed the transmittance dip caused by the Rayleigh Anomaly, together with the two clearly distinct electric and magnetic dipole resonances and a third feature attributed to a high-order Mie resonance. Moreover, the diameter study revealed the appearance of the Kerker effect in the visible, correlated with a narrow spectral range with close to unit transmittance and a 2π phase shift, a feature that was observed for both core-shell structures and TiO_2 metasurfaces with three different refractive index dataset.

For the nonlinear metasurface design, TiO_2-based metasurfaces were first investigated as platform for driving THG at $\lambda_3 = 343$ nm, an option that was later discarded due to the TiO_2 absorption exhibited at the third harmonic exceeding 80% as λ_3 falls at the bandgap edge of the material. The choice then switched toward HfO_2 due to its wider transparency window, with the metasurface simulations showing a more non-local resonance with a ten fold electric field enhancement caused by an overlapping of the magnetic dipole and an electric quadrupole. The metasurface was redesigned to operated in reflection by adding a silver layer under the substrate to maximize the reflection of the first harmonic at 1030 nm. The silver absorption decreased the transmission at the third harmonic down to around 45%.

Two metasurface designs from the diameter study were fabricated on the same chip to study the resonance that appeared close to the Kerker effect. The SEM characterization confirmed the successful fabrication of the intended pillars periodicity, heights and total diameters. However, the ALD tool ran out of TiO_2 precursor during deposition, resulting in pillars with hollow cores of around 39 nm and 43 nm in diameter respectively.

The experimental transmission spectra of the two metasurfaces recorded by the spectrometer did not exhibit the sharp resonant features predicted in the simulations. One of the possible explanation is that the 20 nm spectrometer's resolution spread the transmittance dip of the resonance over a broader spectral range, this hypothesis is consistent with the results shown after applying a 20 nm moving average to the simulated spectra, where the features got broadened and partially suppressed. The modal interference inside the multi-mode fiber may also have played a role in obscuring the resonance, while the incomplete deposition did not affect the appearance of the resonant feature.

Starting from the simulations, this first preliminary work could be improved by directly measuring the actual refractive index values of the deposited material and importing them inside the software to improve the agreement between simulations and experiment and the spectral locations of the resonances. Using a single-mode fiber to collect the light and a higher resolution spectrometer would eliminate the modal interference noise and resolve the narrow resonant features predicted in the simulations, if present. Moreover, the interferometer can enable phase characterization along side transmittance, and an interferometric measurement exploiting both arms of the setup would help in providing a more complete experimental picture of the studied resonances.

In conclusion, future work on the metasurface for third harmonic generation could investigate the response of alternative materials, while the developed design still has to be characterized experimentally to observe THG and validate the field enhancement explored in this work.

References

[1] Minmin Zhu et al. “A general strategy towards controllable replication of butterfly wings for robust light photocatalysis”. In: *Journal of Materials Science and Technology* 105 (2022), pp. 286–292. ISSN: 1005-0302. DOI: https://doi.org/10.1016/j.jmst.2021.07.035. URL: https://www.sciencedirect.com/science/article/pii/S1005030221007775.

[2] R.W. Ziolkowski. “Metamaterials: The early years in the USA”. In: *EPJ Applied Metamaterials* 1 (Jan. 2014), p. 5. DOI: 10.1051/epjam/2014004.

[3] Viktor G Veselago. “THE ELECTRODYNAMICS OF SUBSTANCES WITH SIMULTANEOUSLY NEGATIVE VALUES OF AND ”. In: *Soviet Physics Uspekhi* 10.4 (Apr. 1968), p. 509. DOI: 10.1070/PU1968v010n04ABEH003699. URL: https://doi.org/10.1070/PU1968v010n04ABEH003699.

[4] RA Shelby, D Smith, and S Schultz. “Shelby, R. A., Smith, D. R. Schultz, S. Experimental verification of a negative index of refraction. Science 292, 77-79”. In: *Science (New York, N.Y.)* 292 (May 2001), pp. 77–9. DOI: 10.1126/science.1058847.

[5] Roberto Caputo and Antonio Ferraro. “Metasurfaces: Theoretical Basis and Application Overview”. In: Sept. 2021, pp. 1–20. ISBN: 978-0-7354-2290-2. DOI: 10.1063/9780735422902_001.

[6] “Introduction to Reflectarray Antenna”. In: *Reflectarray Antennas*. John Wiley Sons, Ltd, 2007. Chap. 1, pp. 1–7. ISBN: 9780470178775. DOI: https://doi.org/10.1002/9780470178775.ch1. eprint: https://onlinelibrary.wiley.com/doi/pdf/10.1002/9780470178775.ch1. URL: https://onlinelibrary.wiley.com/doi/abs/10.1002/9780470178775.ch1.

[7] Nanfang yu et al. “Light Propagation with Phase Discontinuities: Generalized Laws of Reflection and Refraction”. In: *Science (New York, N.Y.)* 334 (Sept. 2011), pp. 333–7. DOI: 10.1126/science.1210713.

[8] Francesco Aieta et al. “Aberration-Free Ultrathin Flat Lenses and Axicons at Telecom Wavelengths Based on Plasmonic Metasurfaces”. In: *Nano letters* 12 (Aug. 2012), pp. 4932–6. DOI: 10.1021/nl302516v.

[9] Borui Bian et al. “Novel triple-band polarization-insensitive wide-angle ultra-thin microwave metamaterial absorber”. In: *Journal of Applied Physics* 114 (Nov. 2013), pp. 194511–194511. DOI: 10.1063/1.4832785.

[10] Wenwei Liu et al. “Dielectric Resonance-Based Optical Metasurfaces: From Fundamentals to Applications”. In: *iScience* (Nov. 2020). DOI: 10.1016/j.isci.2020.101868.

[11] Gustav Mie. “Beiträge zur Optik trüber Medien, speziell kolloidaler Metallösungen”. In: *Annalen der Physik* 330.3 (1908), pp. 377–445. DOI: https://doi.org/10.1002/andp.19083300302. eprint: https://onlinelibrary.wiley.com/doi/pdf/10.1002/andp.19083300302. URL: https://onlinelibrary.wiley.com/doi/abs/10.1002/andp.19083300302.

[12] Wei Ting Chen et al. “A broadband achromatic metalens for focusing and imaging in the visible”. In: *Nature Nanotechnology* 13 (Mar. 2018). DOI: 10.1038/s41565-017-0034-6.

[13] Matias Kagias et al. “Metasurface-Enabled Holographic Lithography for Impact-Absorbing Nano-Architected Sheets”. In: *Advanced Materials* 35 (Feb. 2023). DOI: 10.1002/adma.202209153.

[14] Claudio Hail, Lior Michaeli, and Harry Atwater. “Third Harmonic Generation Enhancement and Wavefront Control Using a Local High-Q Metasurface”. In: *Nano letters* 24 (Feb. 2024). DOI: 10.1021/acs.nanolett.3c04476.

[15] Katsuya Tanaka et al. "Femtosecond Pulse Shaping with Semiconductor Huygens' Metasurfaces". In: *Advanced Optical Materials* 13 (Apr. 2025). DOI: 10.1002/adom.202500135.

[16] Wenjun Zhou. "Application of Metasurfaces in Integrated Photonics". In: *Applied and Computational Engineering* 149 (Apr. 2025), pp. 35–44. DOI: 10.54254/2755-2721/2025.KL22355.

[17] Mahdi Shanei. *Optical metasurfaces for momentum exchange between light and matter*. Chalmers Tekniska Hogskola (Sweden), 2025.

[18] Shulin Sun et al. "High-Efficiency Broadband Anomalous Reflection by Gradient Meta-Surfaces". In: *Nano letters* 12 (Nov. 2012). DOI: 10.1021/nl3032668.

[19] Manuel Decker et al. "High-Efficiency Dielectric Huygens' Surfaces". In: *Advanced Optical Materials* 3 (June 2015). DOI: 10.1002/adom.201400584.

[20] Thomas Pertsch and Yuri Kivshar. "Nonlinear optics with resonant metasurfaces". In: *MRS Bulletin* 45 (Mar. 2020), pp. 210–220. DOI: 10.1557/mrs.2020.65.

[21] J. Miragliotta et al. "Linear- and nonlinear-optical properties of GaN thin films". In: *Journal of the Optical Society of America B* 10 (Aug. 1993), pp. 1447–1456. DOI: 10.1364/JOSAB.10.001447.

[22] Sheng Liu et al. "Resonantly Enhanced Second-Harmonic Generation Using III-V Semiconductor All-Dielectric Metasurfaces". In: *Nano Letters* 16 (Aug. 2016). DOI: 10.1021/acs.nanolett.6b01816.

[23] Nils Bernhardt et al. "Quasi-BIC Resonant Enhancement of Second-Harmonic Generation in WS 2 Monolayers". In: *Nano Letters* XXXX (June 2020). DOI: 10.1021/acs.nanolett.0c01603.

[24] Francesco Aieta et al. "Multiwavelength Achromatic Metasurfaces by Dispersive Phase Compensation". In: *Science* (Feb. 2015).

[25] R. Bekenstein et al. "Quantum metasurfaces with atom arrays". In: *Nature Physics* 16 (June 2020), pp. 1–6. DOI: 10.1038/s41567-020-0845-5.

[26] Madona Mekhael et al. "Phase-Matched Second-Harmonic Generation from Metasurfaces Inside Multipass Cells". In: Jan. 2024, STh3P.4. DOI: 10.1364/CLEO_SI.2024.STh3P.4.

[27] Christopher L. Holloway and Edward F. Kuester. "1 - Electromagnetic metamaterials and metasurfaces: historical overview, characterization, and the effect of length scales". In: *Dielectric Metamaterials*. Ed. by Igal Brener et al. Woodhead Publishing Series in Electronic and Optical Materials. Woodhead Publishing, 2020, pp. 1–38. ISBN: 978-0-08-102403-4. DOI: https://doi.org/10.1016/B978-0-08-102403-4.00006-2. URL: https://www.sciencedirect.com/science/article/pii/B9780081024034000062.

[28] Adam Overvig and Andrea Alù. "Diffractive Nonlocal Metasurfaces". In: *Laser Photonics Reviews* 16 (July 2022). DOI: 10.1002/lpor.202100633.

[29] Marina Koledintseva, K.N. Rozanov, and James Drewniak. "Engineering, Modeling and Testing of Composite Absorbing Materials for EMC Applications". In: Mar. 2011. ISBN: 978-953-307-150-3. DOI: 10.5772/14884.

[30] A. Glisson. "Electromagnetic mixing formulas and applications". In: *Antennas and Propagation Magazine, IEEE* 42 (July 2000), pp. 72–73. DOI: 10.1109/MAP.2000.848950.

[31] Zhen Tan et al. "Electromagnetic metagratings for diffraction fields manipulation". In: *Journal of Applied Physics* 138 (Sept. 2025), p. 120701. DOI: 10.1063/5.0250538.

[32] Robert Devlin et al. "Broadband high-efficiency dielectric metasurfaces for the visible spectrum". In: *Proceedings of the National Academy of Sciences of the United States of America* 113 (Sept. 2016). DOI: 10.1073/pnas.1611740113.

[33] You Zhou et al. "Flat optics for image differentiation". In: *Nature Photonics* 14 (May 2020), pp. 1–8. DOI: 10.1038/s41566-020-0591-3.

[34] Nasim Mohammadi Estakhri et al. "Visible Light, Wide-Angle Graded Metasurface for Back Reflection". In: *ACS Photonics* 4 (Jan. 2017). DOI: 10.1021/acsphotonics.6b00965.

[35] Mark Lawrence et al. "High quality factor phase gradient metasurfaces". In: *Nature Nanotechnology* 15 (Nov. 2020), pp. 1–6. DOI: 10.1038/s41565-020-0754-x.

[36] Alexander Sprafke and Jörg Schilling. "9 - Non-resonant dielectric metamaterials". In: *Dielectric Metamaterials*. Ed. by Igal Brener et al. Woodhead Publishing Series in Electronic and Optical Materials. Woodhead Publishing, 2020, pp. 249–288. ISBN: 978-0-08-102403-4. DOI: https://doi.org/10.1016/B978-0-08-102403-4.00014-1. URL: https://www.sciencedirect.com/science/article/pii/B9780081024034000141.

[37] A.J. Cox, Alan DeWeerd, and Jennifer Linden. "An Experiment to Measure Mie and Rayleigh Total Scattering Cross Sections". In: *American Journal of Physics - AMER J PHYS* 70 (June 2002). DOI: 10.1119/1.1466815.

[38] Arseniy Kuznetsov et al. "Optically resonant dielectric nanostructures". In: *Science* 354 (Nov. 2016), aag2472–aag2472. DOI: 10.1126/science.aag2472.

[39] Boris Luk'yanchuk et al. "Optimum Forward Light Scattering by Spherical and Spheroidal Dielectric Nanoparticles with High Refractive Index". In: *ACS Photonics* 2 (June 2015), p. 993. DOI: 10.1021/acsphotonics.5b00261.

[40] Carl Pfeiffer et al. "Efficient Light Bending with Isotropic Metamaterial Huygens' Surfaces". In: *Nano letters* 14 (Apr. 2014). DOI: 10.1021/nl5001746.

[41] Mikhail Limonov et al. "Fano resonances in photonics". In: *Nature Photonics* 11 (Sept. 2017), pp. 543–554. DOI: 10.1038/nphoton.2017.142.

[42] von Neumann J. and Wigner E. "Über merkwürdige diskret Eigenwerte". In: *Phys. Z 30 465* (1929).

[43] Kirill Koshelev, Andrey Bogdanov, and Yuri Kivshar. "Engineering with Bound States in the Continuum". In: *Optics and Photonics News* 31 (Jan. 2020), p. 38. DOI: 10.1364/OPN.31.1.000038.

[44] Yuechen Jia et al. "Surface lattice resonances in dielectric metasurfaces for enhanced light-matter interaction [Invited]". In: *Chinese Optics Letters* 19 (Jan. 2021), p. 060013. DOI: 10.3788/COL202119.060013.

[45] Gabriel Castellanos, Ping Bai, and Jaime Rivas. "Lattice resonances in dielectric metasurfaces". In: *Journal of Applied Physics* 125 (June 2019), p. 213105. DOI: 10.1063/1.5094122.

[46] P. A. Franken, A. E. Hill, and C. Peters. "Generation of Optical Harmonics". In: *Phys. Rev. Lett.* 7 (4 Aug. 1961), pp. 118–119. DOI: 10.1103/PhysRevLett.7.118.

[47] Alex Krasnok, Mykhailo Tymchenko, and Andrea Alù. "Nonlinear Metasurfaces: A Paradigm Shift in Nonlinear Optics". In: *Materials Today* 21 (June 2017). DOI: 10.1016/j.mattod.2017.06.007.

[48] B. Saleh and M. Teich. *Fundamentals of Photonics, 3rd Edition*. Feb. 2019. ISBN: 9781119506874.

[49] R. R. Alfano and S. L. Shapiro. "Emission in the Region 4000 to 7000 Å Via Four-Photon Coupling in Glass". In: *Phys. Rev. Lett.* 24 (11 Mar. 1970), pp. 584–587. DOI: 10.1103/PhysRevLett.24.584.

[50] R. W. Boyd. "Chapter 7 - Processes Resulting from the Intensity-Dependent Refractive Index". In: *Nonlinear Optics (Fourth Edition)*. Ed. by R. W. Boyd. Fourth Edition. Academic Press, 2020, pp. 321–380. ISBN: 978-0-12-811002-7. DOI: https://doi.org/10.1016/B978-0-12-811002-7.00016-3.

[51] J. K. L. MacDonald. "Successive Approximations by the Rayleigh-Ritz Variation Method". In: *Phys. Rev.* (May 1933). DOI: 10.1103/PhysRev.43.830. URL: https://link.aps.org/doi/10.1103/PhysRev.43.830.

[52] J. Jackson. "Electrodynamics, Classical". In: Apr. 2003. ISBN: 3527600434. DOI: 10.1002/3527600434.eap109.

[53] Tatsuki Hinamoto and Minoru Fujii. "MENP: an open-source MATLAB implementation of multipole expansion for nanophotonics". In: *OSA Continuum* 4 (May 2021), pp. 1640–1648. DOI: 10.1364/OSAC.425189.

[54] Swagato Sarkar et al. "Hybridized Guided-Mode Resonances via Colloidal Plasmonic Self-Assembled Grating". In: *ACS Applied Materials Interfaces* 11 (Mar. 2019). DOI: 10.1021/acsami.8b20535.

[55] Mohammad Al-Kuhaili. "Optical Properties of Hafnium Oxide Thin Films and Their Application in Energy-Efficient Windows". In: *Optical Materials* 27 (Dec. 2004), pp. 383–387. DOI: 10.1016/j.optmat.2004.04.014.

[56] Thomas Siefke et al. "Materials Pushing the Application Limits of Wire Grid Polarizers further into the Deep Ultraviolet Spectral Range". In: *Advanced Optical Materials* 4 (July 2016). DOI: 10.1002/adom.201600250.

[57] Ivan Bodurov, Temenuzhka Yovcheva, and Simeon Sainov. "Five-wavelength laser microrefractometer". In: *Optica Applicata* 45 (July 2015), pp. 199–204. DOI: 10.5277/oa150206.

[58] Polina P. Vabishchevich et al. "Enhanced Second-Harmonic Generation Using Broken Symmetry III–V Semiconductor Fano Metasurfaces". In: *ACS Photonics* 5.5 (2018), pp. 1685–1690. DOI: 10.1021/acsphotonics.7b01478. eprint: https://doi.org/10.1021/acsphotonics.7b01478. URL: https://doi.org/10.1021/acsphotonics.7b01478.

[59] A. Brodeur and S. L. Chin. "Ultrafast white-light continuum generation and self-focusing in transparent condensed media". In: *J. Opt. Soc. Am. B* 16.4 (Apr. 1999), pp. 637–650. DOI: 10.1364/JOSAB.16.000637.

[60] A. L. Gaeta. "Catastrophic Collapse of Ultrashort Pulses". In: *Phys. Rev. Lett.* 84 (16 Apr. 2000), pp. 3582–3585. DOI: 10.1103/PhysRevLett.84.3582.

[61] Y. Guozhen and Y. R. Shen. "Spectral broadening of ultrashort pulses in a nonlinear medium". In: *Opt. Lett.* 9.11 (Nov. 1984), pp. 510–512. DOI: 10.1364/OL.9.000510.